Cell Reports
Physical Science

CellPress
OPEN ACCESS

Article

Micro-sized porous bulk bismuth caged by carbon for fast charging and ultralong cycling in sodium-ion batteries

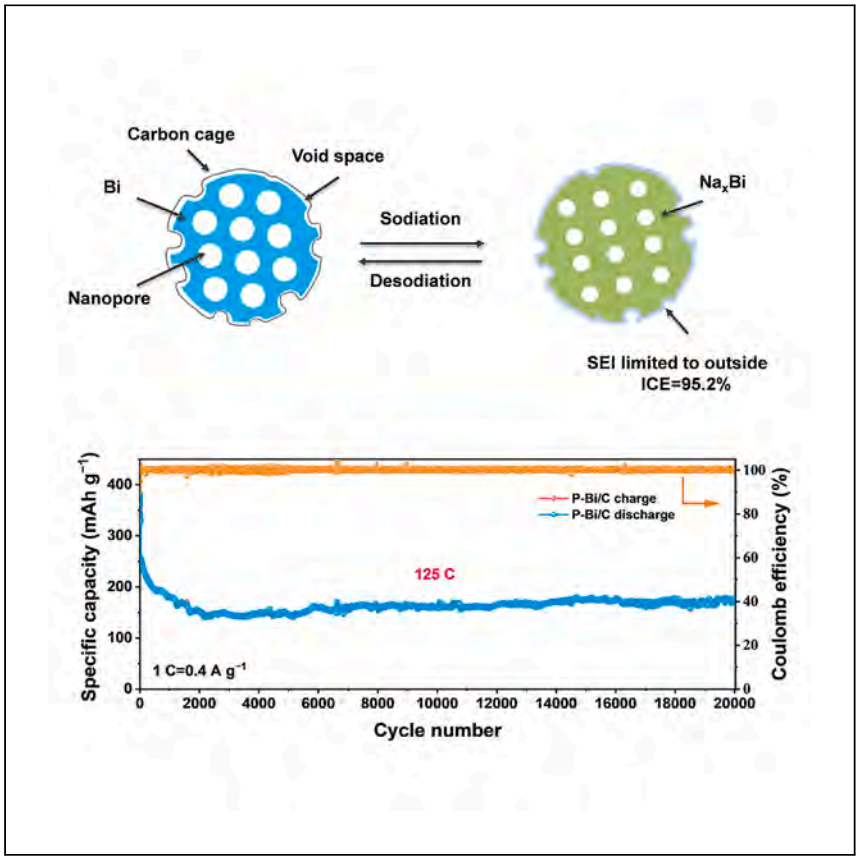

Guo et al. report an anode structure with both nano- and microscale elements for fast-charging sodium-ion batteries. Bicontinuous nanopores and bismuth nanoligaments caged by graphene-like carbon endow a bismuth anode with ultralong cycling and fast-charging capabilities.

Siguang Guo, Changhao Wei, Lei Wang, ..., Biao Gao, Paul K. Chu, Kaifu Huo

gaobiao@wust.edu.cn (B.G.)
kfhuo@hust.edu.cn (K.H.)

Highlights

Porous bulk bismuth caged by carbon contains nanoligaments and bicontinuous nanopores

Bicontinuous pores provide buffer space to accommodate volume expansion in sodium-ion batteries

Reversible formation of hexagonal Na_3Bi phases enable high rate performance

In a full cell, fast charging and ultralong cycles are observed

Guo et al., Cell Reports Physical Science 4, 101463
July 19, 2023
https://doi.org/10.1016/j.xcrp.2023.101463

Cell Reports
Physical Science

CellPress
OPEN ACCESS

Article

Micro-sized porous bulk bismuth caged by carbon for fast charging and ultralong cycling in sodium-ion batteries

Siguang Guo,[1,2,6] Changhao Wei,[1,6] Lei Wang,[2,4,6] Shixiong Mei,[1] Ben Xiang,[1] Yang Zheng,[1] Xuming Zhang,[1] Mehran Javanbakht,[5] Biao Gao,[1,3,*] Paul K. Chu,[3] and Kaifu Huo[2,7,*]

SUMMARY

Bulk bismuth, which has a large tap density and low specific surface area, is considered a promising anode material for sodium-ion batteries. However, bulk bismuth suffers from pulverization upon cycling and sluggish sodium-ion diffusion. Herein, we report micro-sized porous bulk bismuth particles caged by carbon (P-Bi/C) with micro- and nanoscale elements as anodes for sodium-ion batteries. Bicontinuous nanopores provide buffer spaces to accommodate volume expansion of bismuth during cycling, while interconnected bismuth nanoligaments maintain excellent electrochemical stability. Moreover, the reversible formation of NaBi and hexagonal Na_3Bi phases with high sodium-ion diffusivity enables fast electron and ion transport. The P-Bi/C anode has a high initial Coulombic efficiency of 95.2%, a high rate capability of 153.2 mAh g^{-1} at 150C (1C = 400 mA g^{-1}), and excellent cycling stability for over 20,000 cycles. This work aims to advance practical applications for bismuth in fast-charging sodium-ion batteries.

INTRODUCTION

Sodium-ion batteries (SIBs) are promising low-cost alternatives to lithium-ion batteries (LIBs) for large-scale energy storage due to the low cost and abundant sodium resource on the earth.[1] The development of anode materials with high capacity and fast sodiation/desodiation kinetics is highly desirable but still challenging for advanced SIBs because of the larger radius of sodium (Na) ions compared with lithium (Li) ions (1.02 Å for Na^+ vs. 0.76 Å for Li^+).[2,3] Bismuth (Bi) is a promising anode material for fast Na-ion storage because it has a high theoretical volumetric energy density of 3,800 mAh cm^{-3} and high electrical and ionic conductivity.[4] However, the huge volume changes of Bi during repeated sodiation/desodiation processes because of the pulverization of Bi, resulting in rapid capacity decay and poor cyclability.[5]

To address these hurdles, various strategies have been proposed, for example by designing sophisticated nanostructures and embedding the nanosized Bi nanoparticles into a carbon matrix.[6–9] Although nano-Bi or Bi/C composites have been reported to improve cycling stability for Na-ion storage to some extent, they generally have low volumetric capacity and initial Coulombic efficiency (ICE) due to the small tap density and large surface area.[10] Moreover, the expansion of active nano-Bi during cycling inevitably induces large electrode thickness swelling, further reducing the volumetric capacity. In commercial LIBs, a microsized particle is the active material of choice to enable large volumetric energy density and high ICE due to the high

[1]The State Key Laboratory of Refractories and Metallurgy, Institute of Advanced Materials and Nanotechnology, Wuhan University of Science and Technology, Wuhan 430081, China

[2]Wuhan National Laboratory for Optoelectronics (WNLO), School of Optical and Electronic Information, Huazhong University of Science and Technology, Wuhan 430074, China

[3]Department of Physics, Department of Materials Science & Engineering, and Department of Biomedical Engineering, City University of Hong Kong, Tat Chee Avenue, Kowloon, Hong Kong, China

[4]State Key Laboratory of Pulp & Paper Engineering, School of Light Industry and Engineering, South China University of Technology, Guangzhou, China

[5]Department of Chemistry, Amirkabir University of Technology, Tehran, Iran

[6]These authors contributed equally

[7]Lead contact

*Correspondence: gaobiao@wust.edu.cn (B.G.), kfhuo@hust.edu.cn (K.H.)

https://doi.org/10.1016/j.xcrp.2023.101463

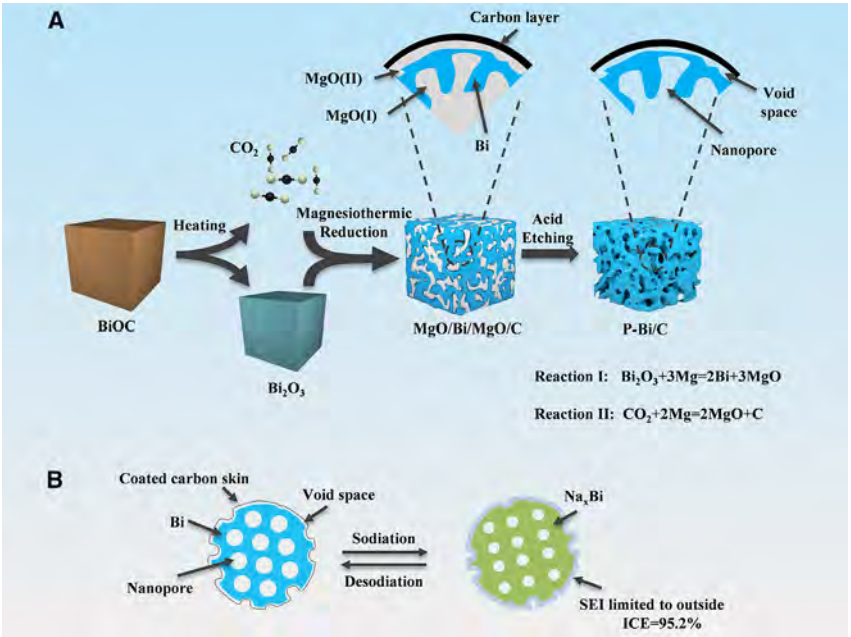

Figure 1. Schematic illustrations of the preparation process and sodiation/desodiation behavior of P-Bi/C

(A) Synthesis process of P-Bi/C.

(B) Schematic illustrating the sodiation/desodiation process of P-Bi/C showing inward volume expansion, stable Bi framework retention, and thin SEI film during cycling.

tap density and small specific surface area.[11,12] However, the microsized Bi particles easily pulverize into small Bi nanoparticles upon sodiation, resulting in losing electrical contact and triggering superfluous growth of solid electrolyte interphase (SEI).[13] Microsized porous Bi could overcome the difficulty faced by nanoscale Bi anodes and show great promise for practical anode materials in SIBs due to the combination of virtues of micro- and nanostructures. However, it remains a huge challenge to fabricate microsized porous Bi with tailored nanoporosity while simultaneously enabling large energy storage, fast kinetics, and long cycling stability because of the low melting point of Bi (271.5°C). On the other hand, the low melting point of Bi makes it difficult to form thin and robust carbon-coating layers to improve the ICE by preventing direct contact between active Na-Bi alloy and the liquid electrolyte.[14]

Herein, we report an efficient one-step strategy for synthesizing microsized porous bulk Bi caged by graphene carbon (denoted as P-Bi/C) as a fast-charging and ultralong life anode material in high-energy SIBs. P-Bi/C is prepared by one-step magnesiothermic reduction (MR) of bismuth carbonate $(BiO)_2CO_3$ (denoted as BiOC) at 500°C under Ar (Figure 1A) followed by acid etching MgO by-product. The porous P-Bi/C particles consisting of interconnected Bi nanoligaments caged by graphene-like carbon and bicontinuous pores afford four advantages for efficient Na-ion storage. First, the interconnected nanoligament network prevents pulverization of Bi upon sodiation and shortens the diffusion distance of Na ions. Moreover, the reversible formation of the NaBi and hexagonal Na_3Bi phases permits high Na-ion diffusivity, therefore resulting in high rate capability. Second, the bicontinuous nanopores provide a pre-engineered inner space to effectively accommodate the expansion of Bi during cycling, enabling a negligible outer expansion at the particle level. Third, the conformal graphene-like carbon cage inhibits the direct contact

between active Na-Bi alloy and the liquid electrolyte and favors the formation of robust and thin NaF-rich SEI with high ion conductivity. Different from the traditional core-shell structure by carbon-coating strategy, there is an interior void of 1–2 nm between the C cage and porous Bi microparticles in P-Bi/C. The interior void provides extra space to accommodate the expansion of Bi during sodiation, therefore giving rise to enhanced structural stability upon sodiation/desodiation (Figure 1B). Fourth, the P-Bi/C particles with sizes of 10–20 μm have a high tap density of 2.55 g cm^{-3} and a small specific surface area of 9.6 m^2 g^{-1}, being beneficial for high volume energy density and large ICE. As a result, the P-Bi/C anode with Bi content of 97% exhibits prominent Na-ion storage performance in terms of a large volumetric capacity of 1,150 mAh cm^{-3}, a high ICE of 95.2%, and ultralong 20,000 cycles at an ultrahigh rate of 125C (1C = 400 mA g^{-1}) with a small capacity loss of 0.0014% per cycle, outperforming the previously reported Bi anode materials (Table S1). Paired with the $Na_3V_2(PO_4)_3$ cathode, the full SIB cell shows a large capacity of 100 mA h g^{-1} and a high energy density of 230 Wh kg^{-1} with 91.1% capacity retention after 1,500 cycles at a current density of 4 A g^{-1}. The rational design strategy of the P-Bi/C anode material contributes to the development of electrode materials with simultaneously improved capacity, rate performance, and cyclability for next-generation high-energy Li/Na-ion batteries.

RESULTS AND DISCUSSION

Synthesis and characterization of P-Bi/C

The preparation procedures of the P-Bi/C composite are schematically illustrated in Figure 1. The commercial BiOC powder is mixed with magnesium (Mg) powder, and then the mixture powder is sealed in a sealed stainless-steel reactor and heated to 500°C for 2 h. During this process, the BiOC firstly pyrolyzes into Bi_2O_3 and CO_2 as demonstrated by the thermogravimetric (TG) analysis (Figure S1). Then, the Mg can react with Bi_2O_3 and CO_2 *in situ* generated via the following two reactions:

$$Bi_2O_3 + 3\ Mg = 2\ Bi + 3\ MgO \quad \text{(Reaction I)}$$

$$CO_2 + 2\ Mg = 2\ MgO + C \quad \text{(Reaction II)}$$

The *in-situ*-generated Bi_2O_3 is firstly reduced by Mg to form MgO and Bi (reaction I), and the graphene-like C produced via reaction II is further deposited on the surface of MgO/Bi to form MgO/Bi/MgO/C composite. The X-ray diffraction (XRD) pattern of the reaction product is depicted in Figure S2. All XRD peaks could be ascribed into the rhombohedral phase of Bi (JCPDS no. 44-1246), MgO (JCPDS no. 45-0946), and Mg_3Bi_2 (JCPDS no. 65-8732). The trace Mg_3Bi_2 is formed due to the side reaction between excess Mg powder (~10%) and Bi. The high-angle annular dark-field (HAADF) scanning transmission electron microscopy (STEM) and high-resolution (HR) TEM images disclose obvious heterointerfaces of MgO/Bi on the nanoscale (Figure S3). The existence of C is proven by Raman spectrum in Figure S4 and energy-dispersive X-ray spectroscopy (EDS) mapping (Figure S5), although the XRD pattern of carbon is not observed due to a low content of 3% (Figure S6). After etching in 1 M hydrochloric acid to remove MgO and trace Mg_3Bi_2, P-Bi/C consisting of bicontinuous pores and interconnected Bi nanoligaments caged by graphene-like C is obtained.

The P-Bi/C particles have a size of 10–20 μm, and SEM images of P-Bi/C are depicted in Figures 2A, 2B, and S7. The Bi nanoligaments have a size of around 100 nm. The Raman shifts at ~69 and ~95.4 cm^{-1} can be attributed to the first-order scattering A_g and E_g modes of Bi.[15] The two broad peaks at 1,345 and 1,574 cm^{-1} correspond

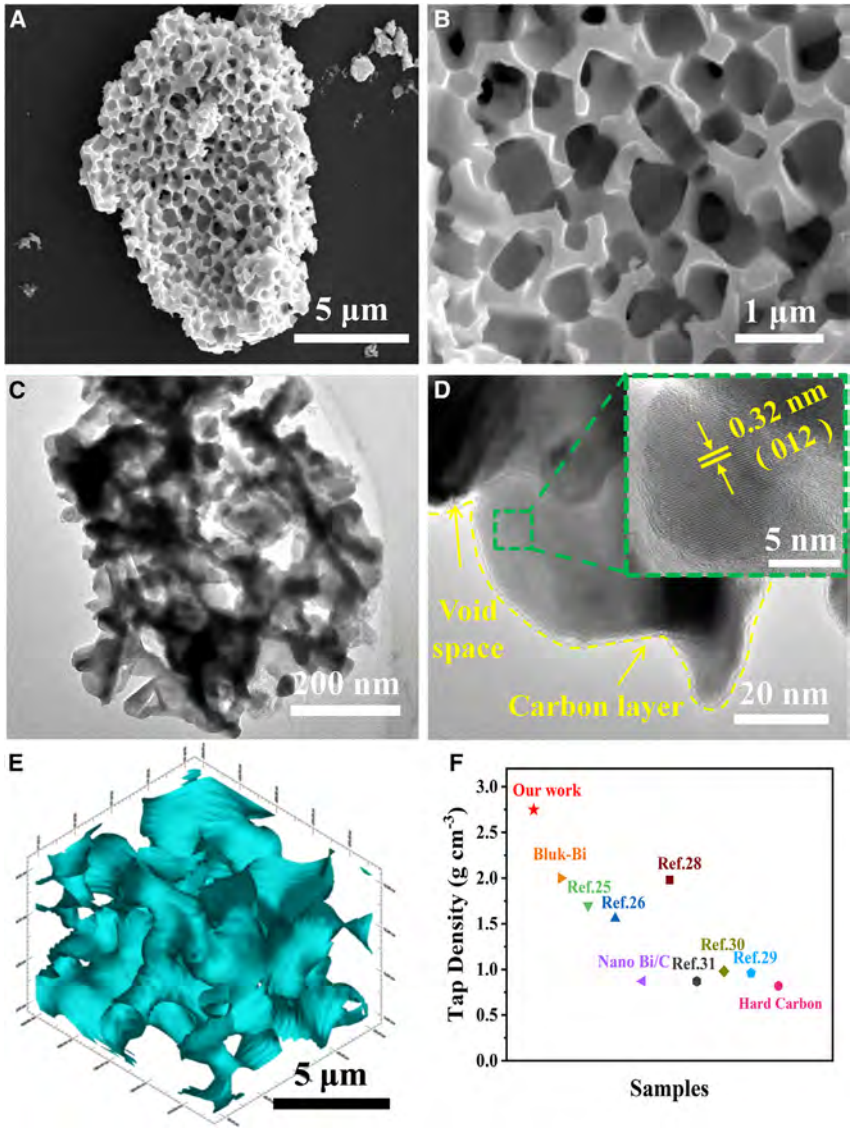

Figure 2. Morphological and structural characterization of P-Bi/C

(A and B) SEM images of P-Bi/C with different magnifications (scale bar for A is 5 μm and for B is 1 μm).

(C and D) TEM (C) and HR-TEM (D) images of P-Bi/C. The reserved interval void between carbon and Bi is clearly identified. The lattice distance of 0.32 nm in the inset corresponds to the (012) planes of rhombohedral Bi (scale bar for C is 200 nm, for D is 20 nm, and for the inset of D is 5 nm).

(E) 3D reconstruction of P-Bi/C (scale bar is 5 μm).

(F) Comparison diagrams of the tap densities of P-Bi/C with previously reported nanostructured Bi, microscale Bi, and other anode materials of SIBs.[19–27]

to the D and G bands of carbon (Figure S8). The small I_D/I_G ratio (0.34) of P-Bi/C discloses a relatively high degree of graphitization.[16] The high-resolution X-ray photoelectron spectroscopy (XPS) spectra of C 1*s* and Bi 4*f* are shown in Figure S9. The Bi 4*f* spectrum exhibits two pairs of peaks at 155.8/161.2 and 158.1/163.4 eV corresponding to metallic Bi and Bi_2O_3.[17] Bi_2O_3 stems from surface oxidization of Bi during air exposure. The four peaks at 284.4, 285, 286.2, and 288.5 eV in the C 1*s* spectrum are attributed to C–C, C–O, C=O, and O–C=O.[18] EDS mapping shows the uniform distribution of Bi and C (Figure S10). TEM images of P-Bi/C are depicted

in Figures 2C and 2D. The lattice distance of 0.32 nm (inset, Figure 2D) corresponds to the (012) plane of rhombohedral phase Bi. Different from the core-shell structure, an obvious 1–2 nm void space between the carbon cage and the Bi particle is observed (Figures 2D and S11), which homogeneously exists on the surface of micro-sized particles and provides extra space to accommodate the expansion of porous Bi during sodiation, further improving structural stability. After removing Bi in aqua regia, the connected C cage with a reserved void space similar to the porous micro-sized Bi size are observed (Figure S12), confirming the formation of a carbon cage. Upon sodiation, the expanded Bi fills the void between two compartments (Figure S13), and the intimate contact between the carbon cage and Bi provide the fast electron transfer pathways.

The porous structure of P-Bi/C is further analyzed by 3D X-ray microscopy combined with the computed tomographic (nano-CT) technique. P-Bi/C is comprised of interconnected Bi nanoligaments and bicontinuous nanopores (Figures 2E and S14), in agreement with TEM and SEM results. The bicontinuous porous structure effectively accommodates volumetric expansion during the sodiation/desodiation process. The P-Bi/C structure has a high tap density of 2.55 g cm^{-3} (Figure S15), which is larger than that of most previously reported nanostructured Bi, microscale Bi, and other anode materials of SIBs (Figure 2G),[19–27] therefore enabling larger volumetric capacity.

Electrochemical properties

The sodium ion storage properties of P-Bi/C are assessed by coin-type half-cells. For comparison, bulk Bi (B-Bi) and porous Bi (P-Bi) are utilized as the control samples. The P-Bi sample is synthesized by MR of commercial Bi_2O_3, which has a similar morphology to P-Bi/C (Figures S16 and S17) but without the carbon cage. The N_2 sorption/desorption isotherms of bulk-Bi, P-Bi, and P-Bi/C are depicted in Figure S18. The Brunauer-Emmett-Teller (BET) surfaces of bulk-Bi, P-Bi, and P-Bi/C are 0.7, 5.6, and 9.6 $m^2\ g^{-1}$, respectively, and the pore sizes of P-Bi/C measured by BET are about 5–7 and 20–30 nm. The increased specific area of 9.6 $m^2\ g^{-1}$ for P-Bi/C compared with that of P-Bi (5.6 $m^2\ g^{-1}$) is ascribed to the dangling bonds of the carbon cage.[28] The initial five cyclic voltammograms (CVs) of P-Bi/C at a scanning rate of 0.1 mV s^{-1} between 0.01 and 1.5 V are depicted in Figure S19. Two pairs of peaks at 0.62/0.76 and 0.48/0.67 V are ascribed to the alloying/dealloying of NaBi and Na_3Bi.[29] The small and broad peak at 0.6 V in the initial CV is associated with the formation of SEI.[30] The anodic and cathodic peaks at 0.62/0.48 and 0.76/0.67 V are overlapped in the first 5 cycles, indicating high reversibility. The plateaus in charging/discharging curves of P/BiC are almost unchanged from the 1^{st} to the 100^{th} cycles (Figure 3A), further confirming the high reversibility of P/BiC during sodiation/desodiation processes. The charging and discharging capacities of P-Bi/C in the initial cycle are 422.2 and 401.7 mAh g^{-1}, boasting an ultrahigh ICE of 95.2%, which is the highest ICE reported so far for Bi-based anodes in SIBs (Figure S20; Table S1). The high ICE of P-Bi/C is associated with the microsized particle and small surface area of 9.6 $m^2\ g^{-1}$. The specific capacities of P-Bi/C at different current densities are depicted in Figure 3B. P-Bi/C has capacities of 369.8, 341.4, 327.6, 307.5, and 274.4 mA h g^{-1} at 1C, 10C, 30C, 50C, and 80C rates, respectively. When the current density is increased by 80-fold from 1C to 80C, 74.3% capacity is retained, suggesting excellent rate capability. Even at an extremely high current density of 180C, P-Bi/C still shows an obvious charging/discharging plateau and a high capacity of 101 mA h g^{-1}, further demonstrating excellent rate capability.

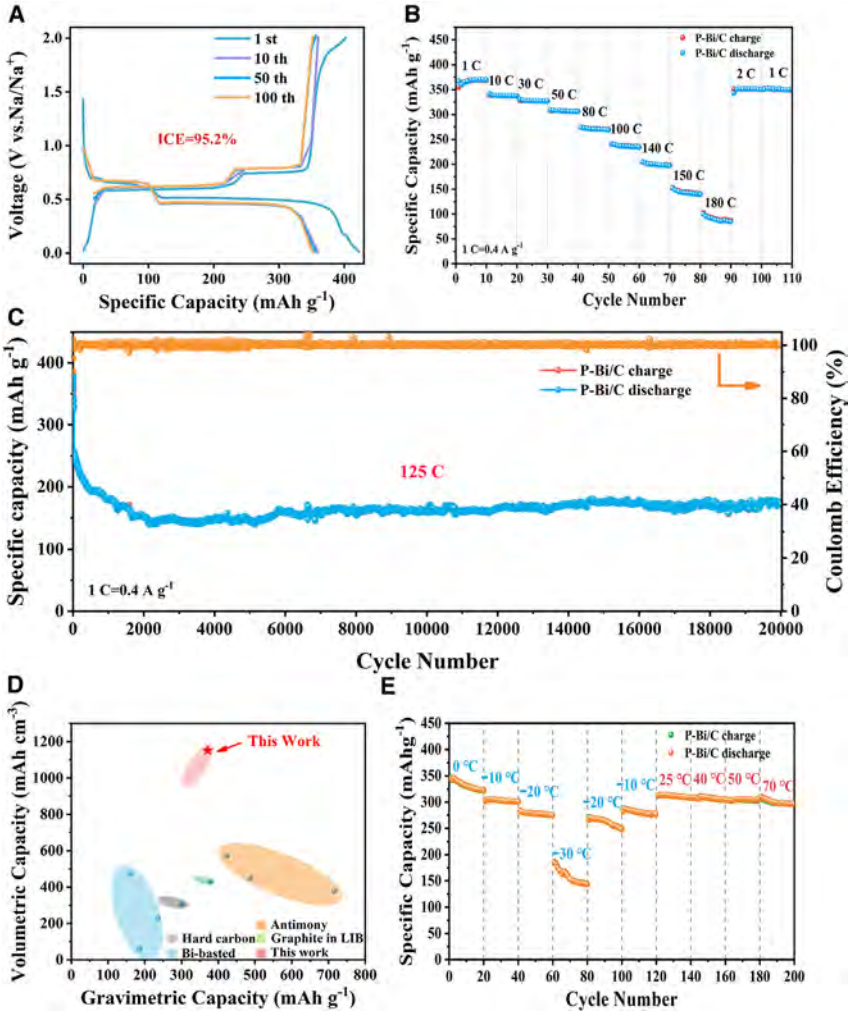

Figure 3. Electrochemical properties of the P-Bi/C composite in half cells.

(A) The 1st, 10th, 50th, and 100th charging/discharging curves at the 1C rate (1C = 400 mA g^{-1}).

(B) Specific capacity at different rates from 1C to 180C.

(C) Cycling performance over 20,000 cycles at 125C with an average capacity loss of 0.0014% per cycle.

(D) Comparison of the volumetric and gravimetric capacities of P-Bi/C with other reported anode materials.[31–41]

(E) The electrochemical properties of P-Bi/C at 10C under different temperatures.

The capacities of P-Bi/C, P-Bi, and B-Bi are 278.1, 222.3, and 146.3 mA h g^{-1} at a current density of 50C after 500 cycles. P-Bi/C shows a larger reversible capacity with 80% capacity retention from the 20th to 500th cycles (Figure S21). Different from the bulk Si anode with poor cyclability due to the pulverization upon lithiation, the spontaneous restructuring of B-Bi in dimethoxyethane (DME) electrolyte via the coalescence of the fragmented Bi nanoparticles (NPs) is beneficial for improving the structural stability,[6] and therefore, the B-Bi particles could be available for over 500 cycles. However, the porous structure via the coalescence of the fragmented Bi NPs is not stable at a high current rate such as 50C, and thus the capacity of B-Bi is decreased to 146.3 mA h g^{-1} with only 50% capacity retention after 500 cycles at 50C. The rate capacity of P-Bi/C from 10C to 100C is superior to that of P-Bi and B-Bi (Figure S22). Remarkably, the P-Bi/C electrode delivers a high capacity of 178

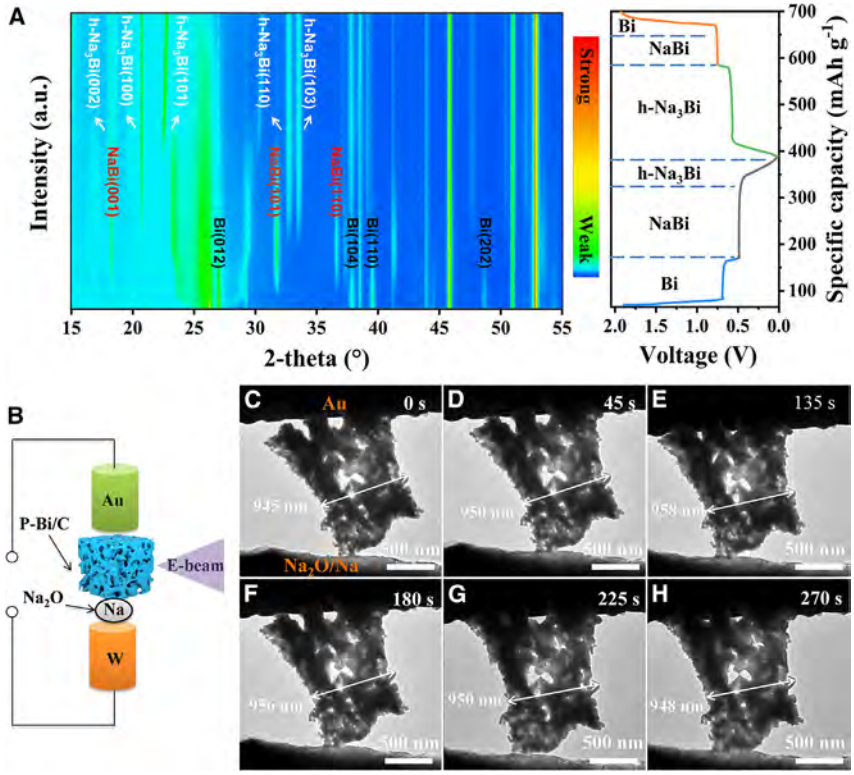

Figure 4. *In situ* XRD and TEM observation of the P-Bi/C upon sodiation/desodiation

(A) *In operando* XRD patterns of the P-Bi/C electrode.

(B) Schematic of the *in situ* nanobattery configuration.

(C–H) Time-resolved *in situ* TEM images during sodiation/desodiation (scale bar is 500 nm; Video S1).

mAh g^{-1} after 20,000 cycles at a large current density of 125C (Figure 3C) with an average capacity loss of 0.0014% per cycle. At a high mass loading of 4.0 mg cm^{-2}, the P-Bi/C anode delivers a specific capacity of 340.1 mAh g^{-1} at a high rate of 10C with 91.8% capacity retention for over 200 cycles (Figure S23). Figure 3D compares the volumetric and gravimetric capacity of P-Bi/C with other reported anode materials for SIBs. P-Bi/C shows a large volumetric capacity of 1,150 mA h cm^{-3} at 1C, which is much higher than that of the reported Bi-based[31–35] and carbon-based[36–41] anode materials, boasting practical applications in fast-charging and high-energy SIBs. The electrochemical properties of P-Bi/C are also evaluated at a wide temperature range (−30°C to 70°C) at 10C (Figure 3E). When the temperature decreases from 25°C to −20°C, the P-Bi/C electrode has only a 9.2% capacity decay. Moreover, P-Bi/C shows an excellent capacity retention of 96.2% from 25°C to 70°C at a high rate of 10C. These results suggest that the P-Bi/C-based SIBs can achieve all-climate application.

In situ XRD and *in situ* TEM characterizations

To better comprehend the mechanism of the fast reaction kinetics, *in situ* XRD and TEM were carried out to observe the structure and phase evolution of the P-Bi/C anode during cycling. The *in situ* XRD results are depicted in Figures 4A and S24, demonstrating reversible conversion of Bi ↔ NaBi ↔ hexagonal Na_3Bi (*h*-Na_3Bi) during alloying/dealloying processes.[42] The *h*-Na_3Bi is a 3D topological Dirac semimetal that has high electron/Na-ion conductivity.[6] During cycling, the large Na-ion

diffusivity and high electric conductivity of NaBi and *h*-Na_3Bi permit fast ion/electron transfer, therefore resulting in fast reaction kinetics and ultrahigh rate capability.

In situ TEM is carried out using a nanobattery (Figure 4B) consisting of gold (Au) probe attached by a single P-Bi/C particle and a Na_2O/Na-coated tungsten (W) probe tip. The Na_2O layer on the surface of Na is employed as the solid electrolyte. The time-resolved TEM images in Figures 4C–4H are captured from the *in situ* videos of sodiation/desodiation (Video S1). The P-Bi/C particles can preserve the porous structure without fracturing. The volume change of P-Bi/C is quantified by the length of the white arrows (Figures 4C–4H) upon sodiation/desodiation. The pristine distance is 945 nm, which slightly elongates to 958 nm at 135 s, corresponding to 0.014% expansion. Upon desodiation, the porous structure of P-Bi/C is retained, and the distance is measured to be 948 nm, demonstrating excellent electrochemical-mechanical stability. Even at a faster charge/discharge via applying −6/6 V bias, the P-Bi/C particle still maintains excellent structural stability and has no notable structural destruction during sodiation/desodiation cycles (Video S2). The *in situ* TEM images in Figure S25 reveal that the pore gradually shrank upon sodiation, confirming that the bicontinuous pores can accommodate the expansion of Bi during sodiation.

Electrode interface evaluation

The interfacial morphology and composition of SEI on the P-Bi/C and P-Bi electrodes after cycling are analyzed by SEM, HR-TEM, and XPS. The P-Bi/C electrode is disassembled after 500 cycles. As shown in Figure S26, the P-Bi/C anode shows a smooth surface and integral structure. Moreover, the electrode swelling is only 8.3% (Figure S27), indicating great promise for practical applications in SIBs. The HR-TEM images after 500 cycles (Figure S28) show that the SEI film of P-Bi/C is thinner, tighter, and smoother compared with P-Bi. XPS is performed using Ar^+ sputtering with a rate of 0.6 nm s^{-1}. The C 1*s* and F 1*s* spectra of the surface of P-Bi/C and P-Bi after 500 cycles are depicted in Figure 5A-B. The peaks at 284.4, 285.2, 289, and 289.2 eV in the C 1*s* XPS spectra of P-Bi/C and P-Bi are ascribed to sodium alkoxides (RCH_2ONa), polyether, RCOONa, and Na_2CO_3, respectively. The existences of RCH_2ONa and Na_2CO_3 are also confirmed by the O 1*s* XPS spectra in Figure S29. The two distinct peaks in the F 1*s* spectrum are assigned to Na-F and P-F.[43] The evolutions of C, O, Na, F, and Bi elements with depth profiling are summarized in Figures 5C and 5D. The higher C and O contents on P-Bi suggest more serious side reactions between the electrolyte and P-Bi. Moreover, the content of F in P-Bi/C is higher than that in P-Bi, implying the formation of F-rich SEI on P-Bi/C. Compared with P-Bi, the organic species is more present in the outer layer, and the inorganic constituents (Na_2O and NaF) are higher in the inner layer for P-Bi/C. The SEI structure on P-Bi and P-Bi/C are schematically shown in Figure 5E. The thin and F-rich SEI on P-Bi/C can facilitate the ion transfer and enable higher mechanical stability, therefore giving rise to enhanced Na-ion storage properties.

The calculated Na ion diffusion coefficient (D_{Na^+}) of P-Bi/C from the galvanostatic intermittent titration technique (GITT) curves is nearly two orders of magnitude larger than that of P-Bi (Figure S30). The uniform NaF in SEI on the P-Bi/C surface permit the rapid transport of Na ions, resulting in improved rate capability.[44] Electrochemical impedance spectroscopy (EIS) is performed to quantitatively analyze the interface impedance and Na^+ ion diffusion of the P-Bi/C electrode (Figure S31). The calculated contact resistance (*Rs*) and charge-transfer resistance (*Rct*) are shown in Table S2. The low *Rct* of P-Bi/C is indicative of fast charge transfer.

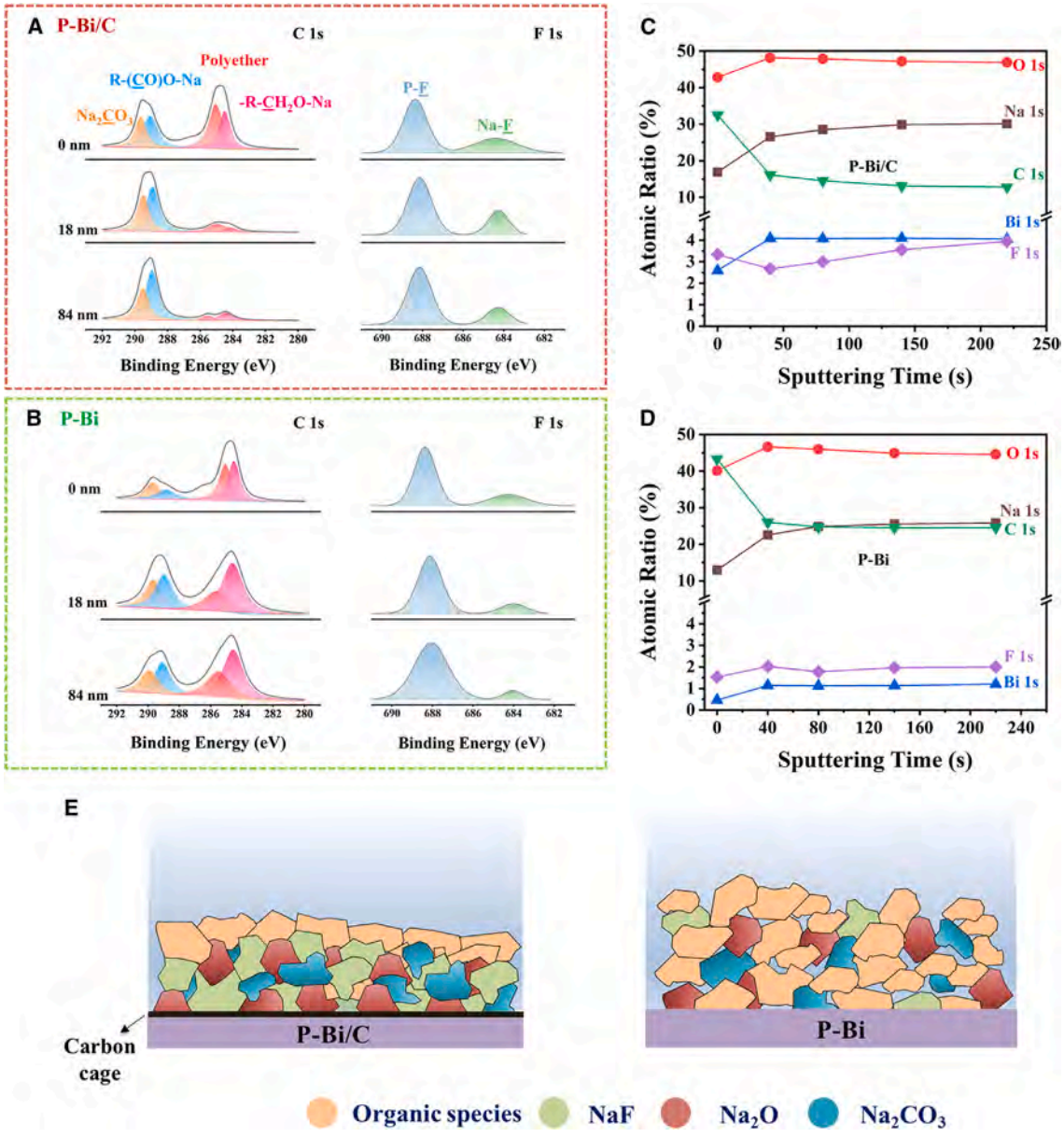

Figure 5. Interfacial morphology and chemical composition after cycling

(A and B) C 1s and F 1s XPS spectra of P-Bi/C (A) and P-Bi (B) after Ar ion sputtering with different depths.

(C and D) The evolutions of C, O, Na, F, and Bi elements with depth profiling in P-Bi/C (C) and P-Bi (D) electrodes.

(E) Schematic illustration of the SEI layers on P-Bi/C and P-Bi, revealing the thin and robust F-rich SEI on the P-Bi/C surface.

Full cell evaluation

The practical implementation of the P-Bi/C anode is further evaluated by a full battery with $Na_3V_2(PO_4)_3$ (NVP) as the cathode (denoted as P-Bi/C//NVP), as shown in Figure 6A. The initial desodiation and sodiation capacities for the NVP cathode are 133 and 116 mAh g^{-1}, corresponding to an ICE of 87%. The NVP half-cell also delivers a high reversible capacity of 117 mAh g^{-1} at 0.1 A g^{-1} with high capacity retention of 99% from the 2nd to 100th cycles (Figure S32). The P-Bi/C//NVP battery is tested between 2.2 and 3.3 V, and the negative/positive (n/p) ratio of P-Bi/C//NVP is 1.1. The CV curve at a scanning rate of 0.1 mV s^{-1} reveals two pairs of redox

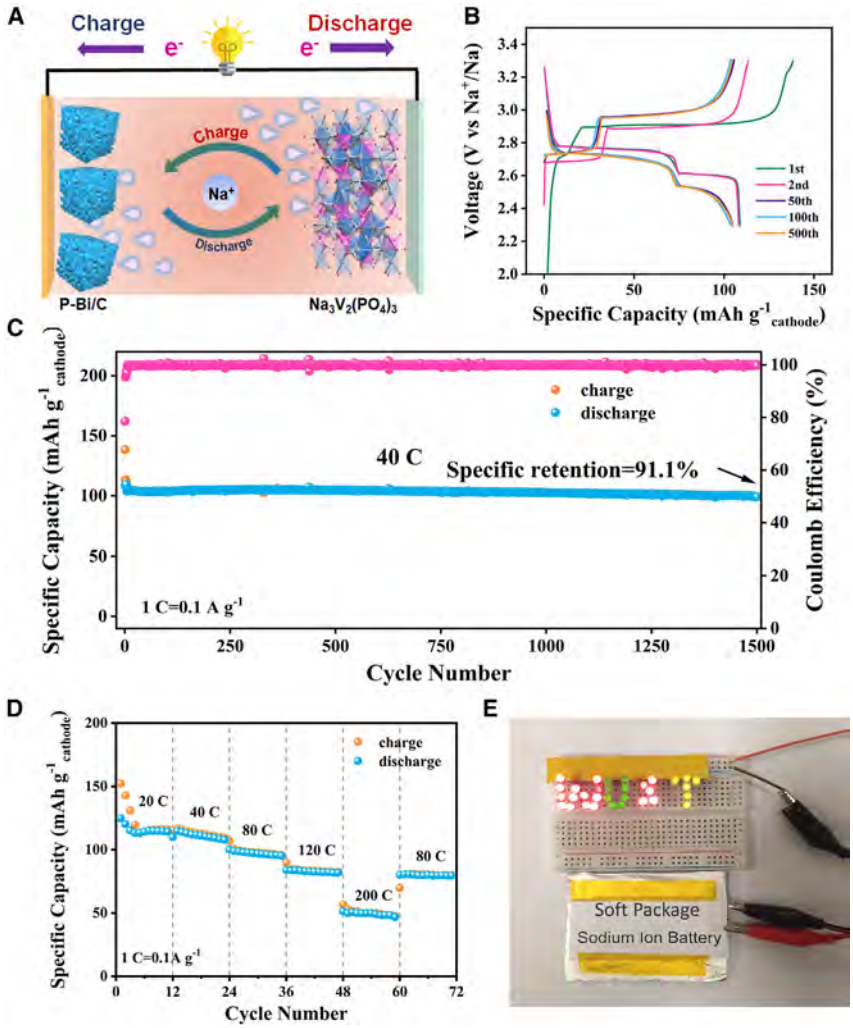

Figure 6. Electrochemical properties of the P-Bi/C//NVP full cells

(A) Schematic illustration of the device.

(B) Charging/discharging curves of the 1st, 2nd, 50th, 100th, and 500th cycles at 10C rate (1C = 100 mA g^{-1}).

(C) Cycling properties.

(D) Capacities at different rates.

(E) Photograph of the pouch full cell to power LED lights.

peaks at 2.53/2.65 and 2.75/3.01 V, which corresponds to the redox reaction of V^{4+}/V^{3+} and Na^+ insertion/extraction processes. The CV curves at the 1st, 2nd, and 5th cycles are overlapped, indicating good reversibility (Figure S33). The charging/discharging plots of P-Bi/C//NVP show a stable and reversible capacity of 110 mA h g^{-1} at 40C (1C = 0.1 A g^{-1}), and the charging/discharging plots are overlapped within 500 cycles, indicating high reversibility (Figure 6B). As shown in Figure 6C, the P-Bi/C//NVP full cell delivers a high reversible capacity of 100 mAh g^{-1} at 40C and a large energy density of 230 Wh kg^{-1} with capacity retention of 91.1% after 1,500 cycles, outperforming the $LiFePO_4$//graphite-based LIBs and most SIBs. Moreover, the full cell still delivers a high capacity of 50 mAh g^{-1} even at 200C (Figure 6D), manifesting a robust rate performance and fast-charging capability. Notably, the P-Bi/C//NVP soft pack battery can fully power a series of LED lamps (2.7 V) (Figure 6E), illustrating their practical feasibility. These

results confirm that P-Bi/C could constitute a desirable platform for advanced SIBs with high power/energy densities and long-term stability.

In summary, microsized porous Bi particles caged by carbon have been prepared by one-step MR of BiOC at 500°C followed by acid etching an *in-situ*-generated MgO template. The bicontinuous nanopores provide buffer spaces to accommodate volume expansion of Bi during cycling, therefore enabling negligible outer expansion at the particle level, while the 3D interconnected Bi nanoligaments maintain excellent electrochemical and structural stability. Moreover, the conformal graphene-like carbon cage facilitates fast electron transfer kinetics and favors the formation of robust and thin NaF-rich SEI with high ion conductivity. The high conductivity, short ion diffusion distance of Bi nanoligaments and the reversible formation of the NaBi and *h*-Na_3Bi phases with high Na-ion diffusivity permit the fast electron/ion transport, therefore resulting in the fast-charging capability of P-Bi/C. P-Bi/C shows an impressive electrochemical performance in terms of an ultrahigh volumetric capacity of 1,150 mA h cm^{-3}, a large ICE of 95.2%, and ultralong-term stability over 20,000 cycles at an extremely high current density of 125C with an average capacity loss of 0.0014% per cycle. The strategy to construct microsized porous P-Bi/C particles has large potential in fast-charging and ultralong-life Na-ion batteries.

EXPERIMENTAL PROCEDURES

Resource availability

Lead contact

Further information and requests for resources and reagents should be directed to and will be fulfilled by the lead contact, Kaifu Huo (kfhuo@hust.edu.cn).

Materials availability

All materials in this study will be made available from the lead contact upon reasonable request.

Data and code availability

All data are provided in the article and supplemental information, and any additional information needed can be obtained from the lead contact upon reasonable request.

Material synthesis

P-Bi/C was prepared via a MR route. Firstly, 2 g BiOC and 0.5 g magnesium powder were mixed and transferred to a sealed stainless-steel autoclave and heated to 500°C for 2 h under Ar. After cooling to room temperature naturally, the product was taken out and washed with 1 M hydrochloric acid and distilled water 3 times to remove the MgO by-product. The samples were centrifuged and dried overnight to obtain the P-Bi/C powder. The control sample of P-Bi was prepared by the same method as P-Bi/C, except that BiOC was replaced by the commercial Bi_2O_3 powder.

Materials characterizations

The micromorphology and structure of the samples were examined by field-emission SEM (FE-SEM; Apreo S HiVac), HR-TEM (JEM-2100F), and STEM (FEI Titan G2) with EDS (Aztec Ultim Live 100X). The porous structure was evaluated by nano-CT (GE vtomax) and nitrogen adsorption-desorption isotherms on the BET instrument (Micrometrics, TriStar II 3flex) at 77 K after degassing at 423 K for 8 h. The phase and composition of the samples were determined by XRD (Smart Lab SE) using Cu K_α radiation (λ = 0.15406 nm) in the 2θ range from 10° to 90°. Fourier

transform infrared (FTIR) spectroscopy (Nicolet 460) and Raman scattering using an excitation wavelength of 532 nm (Horiba HR revolution), as well as XPS (AXIS SUPRA+, Kratos) were performed to analyze the composite and chemical states. The MR mechanism and C concentration in P-Bi/C was determined by TG (TA449/6/GNETZSCH) and differential thermal analysis (DTA) from 30°C to 900°C using a heating rate of 5°C min^{-1} in air or Ar.

Electrochemical measurements

The samples were evaluated in a 2032-type coin cell and a soft-packet full cell, respectively. The electrode film was fabricated by the typical doctor blade method by pasting the electrode slurry on the Cu foil with mass loadings on the electrode of 1.4–4 mg cm^{-2}. The slurry was composed of the active materials, carbon black, and sodium alginate in an aqueous solution with a mass ratio of 7:1.5:1.5. The ultimate electrode was dried at 70°C in vacuum oven. The CR2032-type coin cells were assembled in a glove box (Vigor SG1200/750TS-C) with glass fiber (GF/D) as the separator and Na metal as the counter electrodes. The electrolyte was 1 M sodium hexafluorophosphate ($NaPF_6$) in DME. The electrochemical measurements were carried out on the battery tester LANDCT2001A (Wuhan LAND Electronics, Wuhan, China). CV and EIS were conducted on the CHI750e electrochemical workstation (Shanghai CH Instrument Company, Shanghai, China).

SUPPLEMENTAL INFORMATION

Supplemental information can be found online at https://doi.org/10.1016/j.xcrp.2023.101463.

ACKNOWLEDGMENTS

This work was financially supported by the National Key R&D Program of China (2022VFB2404800), the National Natural Science Foundation of China (nos. U2004210, 51974208, and U2003130); the Application Foundation Frontier Project of Wuhan City (2020010601012199); the Outstanding Youth Foundation of Natural Science Foundation of Hubei Province (2020CFA099); the Innovation Group of the Natural Science Foundation of Hubei Province (2019CFA020); the Knowledge Innovation Project of Wuhan City (2022010801010303); the Shenzhen-Hong Kong Innovative Collaborative Research and Development Program (SGLH20181109110802117 and CityU9240014); and a City University of Hong Kong Donation Research Grant (DON-RMG no. 9229021). The authors are grateful to the facility support provided by the Analytical and Testing Center of HUST.

AUTHOR CONTRIBUTIONS

S.G., B.G., and K.H. conceived this idea and designed the experiments. S.G., C.W., and L.W. performed the materials synthesis and electrochemical measurements. S.M., B.X., Y.Z., M.J., and X.Z. conducted the characterization and data analysis. S.G., B.G., P.K.C., and K.H. wrote the paper. P.K.C. revised the manuscript. All authors discussed the results and contributed to preparing the manuscript.

DECLARATION OF INTERESTS

The authors declare no competing interests.

Received: January 9, 2023
Revised: March 30, 2023
Accepted: May 31, 2023
Published: June 22, 2023

REFERENCES

1. Vaalma, C., Buchholz, D., Weil, M., and Passerini, S. (2018). A cost and resource analysis of sodium-ion batteries. Nat. Rev. Mater. *3*, 18013.
2. Feng, X., Fang, H., Wu, N., Liu, P., Jena, P., Nanda, J., and Mitlin, D. (2022). Review of modification strategies in emerging inorganic solid-state electrolytes for lithium, sodium, and potassium batteries. Joule *6*, 543–587.
3. Li, Y., Zhou, Q., Weng, S., Ding, F., Qi, X., Lu, J., Li, Y., Zhang, X., Rong, X., Lu, Y., et al. (2022). Interfacial engineering to achieve an energy density of over 200 Wh kg^{-1} in sodium batteries. Nat. Energy *7*, 511–519.
4. Chayambuka, K., Mulder, G., Danilov, D.L., and Notten, P.H.L. (2018). Sodium-ion battery materials and electrochemical properties reviewed. Adv. Energy Mater. *8*, 1800079.
5. Liang, Y., Song, N., Zhang, Z., Chen, W., Feng, J., Xi, B., and Xiong, S. (2022). Integrating Bi@ C nanospheres in porous hard carbon frameworks for ultrafast sodium storage. Adv. Mater. *34*, 2202673.
6. Kim, Y.H., An, J.H., Kim, S.Y., Li, X., Song, E.J., Park, J.H., Chung, K.Y., Choi, Y.S., Scanlon, D.O., Ahn, H.J., and Lee, J.C. (2022). Enabling 100C fast-charging bulk Bi anodes for Na-ion batteries. Adv. Mater. *34*, 2201446.
7. Hong, W., Wang, A., Li, L., Qiu, T., Li, J., Jiang, Y., Zou, G., Peng, H., Hou, H., and Ji, X. (2021). Bi dots confined by functional carbon as high-performance anode for lithium-ion batteries. Adv. Funct. Mater. *31*, 2000756.
8. Xiong, P., Bai, P., Li, A., Li, B., Cheng, M., Chen, Y., Huang, S., Jiang, Q., Bu, X.H., and Xu, Y. (2019). Bismuth nanoparticle@ carbon composite anodes for ultralong cycle life and high-rate sodium-ion batteries. Adv. Mater. *31*, 1904771.
9. Sun, Z., Liu, Y., Ye, W., Zhang, J., Wang, Y., Lin, Y., Hou, L., Wang, M., and Yuan, C. (2021). Unveiling intrinsic potassium storage behaviors of hierarchical nano Bi@ N-doped carbon nanocages framework via in situ characterizations. Angew. Chem. Int. Ed. Engl. *133*, 7256–7263.
10. Jain, R., Lakhnot, A.S., Bhimani, K., Sharma, S., Mahajani, V., Panchal, R.A., Kamble, M., Han, F., Wang, C., and Koratkar, N. (2022). Nanostructuring versus microstructuring in battery electrodes. Nat. Rev. Mater. *7*, 736–746.
11. Cheng, X., Shao, R., Li, D., Yang, H., Wu, Y., Wang, B., Sun, C., Jiang, Y., Zhang, Q., and Yu, Y. (2021). A self-healing volume variation three-dimensional continuous bulk porous bismuth for ultrafast sodium storage. Adv. Funct. Mater. *31*, 2011264.
12. An, W., Gao, B., Mei, S., Xiang, B., Fu, J., Wang, L., Zhang, Q., Chu, P.K., and Huo, K. (2019). Scalable synthesis of ant-nest-like bulk porous silicon for high-performance lithium-ion battery anodes. Nat. Commun. *10*, 1447.
13. Zheng, S.M., Tian, Y.R., Liu, Y.X., Wang, S., Hu, C.Q., Wang, B., and Wang, K.M. (2021). Alloy anodes for sodium-ion batteries. Rare Met. *40*, 272–289.
14. Zeng, Y., Lin, Z., Wang, Z., Wu, M., Tong, Y., and Lu, X. (2018). In situ activation of 3D porous Bi/carbon architectures: toward high-energy and stable nickel-bismuth batteries. Adv. Mater. *30*, 1707290.
15. Zhou, J., Chen, J., Chen, M., Wang, J., Liu, X., Wei, B., Wang, Z., Li, J., Gu, L., Zhang, Q., et al. (2019). Few-layer bismuthene with anisotropic expansion for high-areal-capacity sodium-ion batteries. Adv. Mater. *31*, 1807874.
16. Yang, Z., Chen, T., Chen, D., Shi, X., Yang, S., Zhong, Y., Liu, Y., Wang, G., Zhong, B., Song, Y., et al. (2021). A Ge/carbon atomic-scale hybrid anode material: a micro–nano gradient porous structure with high cycling stability. Angew. Chem. Int. Ed. Engl. *60*, 12539–12546.
17. Qin, T., Wang, D., Zhang, X., Wang, Y., Drewett, N.E., Zhang, W., Dong, T., Li, T., Wang, Z., Deng, T., et al. (2021). Unlocking the optimal aqueous δ-Bi_2O_3 anode via unifying octahedrally liberated Bi-atoms and spilled nano-Bi exsolution. Energy Stor. Mater. *36*, 376–386.
18. Yang, H., Chen, L.W., He, F., Zhang, J., Feng, Y., Zhao, L., Wang, B., He, L., Zhang, Q., and Yu, Y. (2020). Optimizing the void size of yolk-Shell Bi@ void@ C Nanospheres for high-power-density sodium-ion batteries. Nano Lett. *20*, 758–767.
19. Wang, C., Wang, L., Li, F., Cheng, F., and Chen, J. (2017). Bulk bismuth as a high-capacity and ultralong cycle-life anode for sodium-ion batteries by coupling with glyme-based electrolytes. Adv. Mater. *29*, 1702212.
20. He, X.D., Liao, J.Y., Wang, S., Wang, J.R., Liu, Z.H., Ding, X., Hu, Q., Wen, Z.Y., and Chen, C.H. (2019). From nanomelting to nanobeads: nanostructured $Sb_x Bi_{1-x}$ alloys anchored in three-dimensional carbon frameworks as a high-performance anode for potassium-ion batteries. J. Mater. Chem. *7*, 27041–27047.
21. Sun, D., Zhang, G., Li, D., Liu, S., Jia, X., and Zhou, J. (2019). A layered Bi_2Te_3 nanoplates/graphene composite with high gravimetric and volumetric performance for Na-ion storage. Sustain. Energy Fuels *3*, 3163–3171.
22. Wen, Y., He, K., Zhu, Y., Han, F., Xu, Y., Matsuda, I., Ishii, Y., Cumings, J., and Wang, C. (2014). Expanded graphite as superior anode for sodium-ion batteries. Nat. Commun. *5*, 4033.
23. Cheng, D., Yang, L., Hu, R., Liu, J., and Zhu, M. (2021). Microsized SnS/few-layer graphene composite with interconnected nanosized building blocks for superior volumetric lithium and sodium storage. Energy Environ. Mater. *4*, 229–238.
24. Tian, W., Wang, L., Huo, K., and He, X. (2019). Red phosphorus filled biomass carbon as high-capacity and long-life anode for sodium-ion batteries. J. Power Sources *430*, 60–66.
25. Zhang, N., Liu, Y., Lu, Y., Han, X., Cheng, F., and Chen, J. (2015). Spherical nano-Sb@ C composite as a high-rate and ultra-stable anode material for sodium-ion batteries. Nano Res. *8*, 3384–3393.
26. Liu, L., Shi, R., Li, Y., Wu, Y., Ye, K., Yan, X., Shi, Y., and Cao, C. (2018). In situ constructing MoS_2-C nanospheres as advanced anode for sodium-ion battery. ChemistrySelect *3*, 11381–11387.
27. Yuan, H., Jin, Y., Chen, X., Lan, J., Yu, Y., and Yang, X. (2019). Large-scale fabrication of egg-carton-inspired Bi/C composite toward high volumetric capacity and long-life lithium ion batteries. ACS Sustain. Chem. Engin. *7*, 6033–6042.
28. Wang, X.P., Qi, X.F., Yang, B., Chen, S.Y., Wang, J.Y., Zhao, J., Pei, A., Tang, J., Zheng, X., Chen, W., and Cui, Y. (2019). Surface-engineered mesoporous silicon microparticles as high-Coulombic-efficiency anodes for lithium-ion batteries. Poult. Sci. *98*, 404–412.
29. Wang, A., Hong, W., Yang, L., Tian, Y., Qiu, X., Zou, G., Hou, H., and Ji, X. (2020). Bi-based electrode materials for alkali metal-ion batteries. Small *16*, 2004022.
30. Cheng, X., Li, D., Wu, Y., Xu, R., and Yu, Y. (2019). Bismuth nanospheres embedded in three-dimensional (3D) porous graphene frameworks as high performance anodes for sodium-and potassium-ion batteries. J. Mater. Chem. A *7*, 4913–4921.
31. Li, Y., Zhong, X., Wu, X., Li, M., Zhang, W., and Wang, D. (2021). Bi/C nanosheet microspheres with an open pore structure as anodes for sodium ion batteries with high capacity, excellent rate performance and long cycle life. J. Mater. Chem. A *9*, 22364–22372.
32. Qi, S., Xie, X., Peng, X., Ng, D.H.L., Wu, M., Liu, Q., Yang, J., and Ma, J. (2019). Mesoporous carbon-coated bismuth nanorods as anode for potassium-ion batteries. Phys. Status Solidi Rapid Res. Lett. *13*, 1900209.
33. Chen, J.M., Fan, X., Ji, X., Gao, T., Hou, S., Zhou, X., and Wang, C. (2018). Intercalation of Bi nanoparticles into graphite results in an ultra-fast and ultra-stable anode material for sodium-ion batteries. Energy Environ. Sci. *156*, 1218–1219.
34. Li, D., Zhou, J., Chen, X., and Song, H. (2018). Graphene-loaded Bi_2Se_3: a conversion-alloying-type anode material for ultrafast gravimetric and volumetric Na storage. ACS Appl. Mater. Interfaces *10*, 30379–30387.
35. Park, B., Lee, S., Han, D.Y., Jang, H., Gi Seong, D., Yoo, J.K., Park, S., Oh, Y., and Ryu, J. (2023). Multiscale hierarchical design of bismuth-carbon anodes for ultrafast-charging sodium-ion full battery. Appl. Surf. Sci. *614*, 156188.
36. Lu, Z., Geng, C., Yang, H., He, P., Wu, S., Yang, Q.H., and Zhou, H. (2022). Step-by-step desolvation enables high-rate and ultra-stable

sodium storage in hard carbon anodes. Proc. Natl. Acad. Sci. USA *119*, e2210203119.

37. Chen, Y., Hu, X., Evanko, B., Sun, X., Li, X., Hou, T., Cai, S., Zheng, C., Hu, W., and Stucky, G.D. (2018). High-rate FeS_2/CNT neural network nanostructure composite anodes for stable, high-capacity sodium-ion batteries. Nano Energy *46*, 117–127.

38. Liu, Y., Fang, Y., Zhao, Z., Yuan, C., and Lou, X.W.D. (2019). A ternary $Fe_{1-x}S$@porous carbon nanowires/reduced graphene oxide hybrid film electrode with superior volumetric and gravimetric capacities for flexible sodium ion batteries. Adv. Energy Mater. *9*, 1803052.

39. Liu, J., Liu, C.S., Ye, X.J., and Yan, X.H. (2018). Monolayer InP_3 as a reversible anode material for ultrafast charging lithium-and sodium-ion batteries: a theoretical study. J. Mater. Chem. *6*, 3634–3641.

40. Vo, T.N., Kim, D.S., Mun, Y.S., Lee, H.J., Ahn, S.k., and Kim, I.T. (2020). Fast charging sodium-ion batteries based on Te-PC composites and insights to low-frequency limits of four common equivalent impedance circuits. Chem. Eng. J. *398*, 125703.

41. Nitta, N., Wu, F., Lee, J.T., and Yushin, G. (2015). Li-ion battery materials: present and future. Mater. Today *18*, 252–264.

42. Zhang, Z., Wang, R., Zeng, J., Shi, K., Zhu, C., and Yan, X. (2021). Size effects in sodium ion batteries. Adv. Funct. Mater. *31*, 2106047.

43. Ma, M., Cai, H., Xu, C., Huang, R., Wang, S., Pan, H., and Hu, Y. (2021). Engineering solid electrolyte interface at nano-scale for high-performance hard carbon in sodium-ion batteries. Adv. Funct. Mater. *31*, 2100278.

44. Zhang, X., Wang, D., Qiu, X., Ma, Y., Kong, D., Müllen, K., Li, X., and Zhi, L. (2020). Stable high-capacity and high-rate silicon-based lithium battery anodes upon two-dimensional covalent encapsulation. Nat. Commun. *11*, 3826.

Cell Reports Physical Science, Volume *4*

Supplemental information

Micro-sized porous bulk bismuth caged by carbon for fast charging and ultralong cycling in sodium-ion batteries

Siguang Guo, Changhao Wei, Lei Wang, Shixiong Mei, Ben Xiang, Yang Zheng, Xuming Zhang, Mehran Javanbakht, Biao Gao, Paul K. Chu, and Kaifu Huo

Supplemental Experimental Procedures

In-situ TEM

In-situ TEM was performed on P-Bi/C using a typical nanobattery system with P-Bi/C single micro-particle as the working electrode, metallic Na particles with a naturally grown Na_2O layer as the counter electrode, and a solid electrolyte. The micro-sized P-Bi/C particles were scratched by a gold wire and a tungsten tip was used to scratch the Na particles in a glove box (Vigor SG1200/750TS-C). The gold wire with P-Bi/C micro-sized particles on the tip was transferred to the TEM-scanning tunneling microscopy (STM) specimen holder. The tungsten tip with Na particles on top was inserted into the holder. The holder with P-Bi/C particles and Na particles was rapidly transferred to the TEM instrument (JEOL-2100). During the process, a thin Na_2O layer was formed on the Na surface due to controllable air exposure to simulate commercial assembly of nano-batteries. Voltages of −3/3 and −6/6 V were applied to the two electrodes of the nano-battery for sodiation/desodiation.

In-situ XRD

In-situ XRD experiment was conducted in a home-made *in situ* XRD cell, and a P-Bi/C slurry was coated onto carbon paper in an argon-filled glove-box, where beryllium (Be) was used as an X-ray transmissive window. The *in-situ* XRD was characterized on a SmartLab instrument (Rigaku) with filtered Cu Kα radiation (λ = 0.15406 nm) in the 2 θ range from 10 ° to 90 ° at a scanning speed of 10 °min^{-1}.

The soft-packet full cell of P-Bi/C consisted of the NVP cathode materials as described previously.[1] The P-Bi/C anode and NVP cathode were paired with the DME electrolyte to obtain the soft-packet cell labeled as Bi/C//NVP. The electrochemical properties of Bi/C//NVP was evaluated by galvanostatic charging/discharging between 2.8 V and 4.25 V at 2 C (1 C= 0.1 A g^{-1}) and the energy density of the Bi/C//NVP was calculated based on the weight of the active materials of Bi/C and NVP. Calculation of the ideal energy density was based on the reversible capacity of the cathode and anode in the full cell with the n/p ratio set to be 1.1 can be estimated according to the equation:

Energy Density $Em = \frac{E}{m} = \int \frac{QdV}{m} = \int \frac{Q}{m} dV$

Where Q is the capacity of the P-Bi/C//NVP, V is the potential for the discharge process, m is the mass of active materials in electrodes.

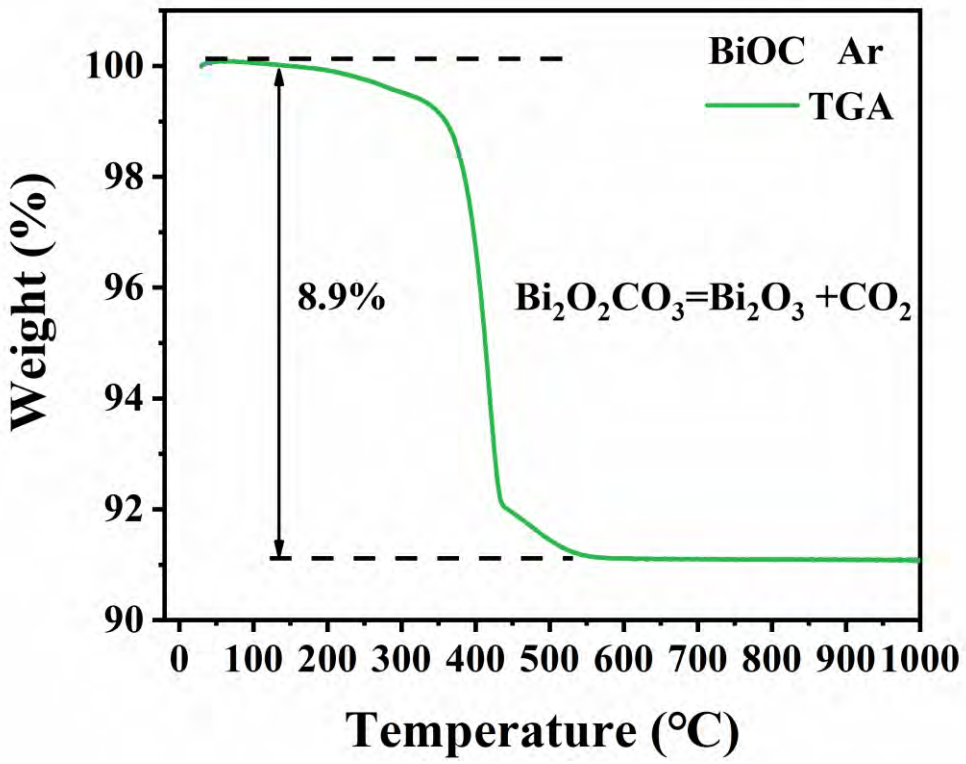

Figure S1. TGA curves of BiOC under Ar.

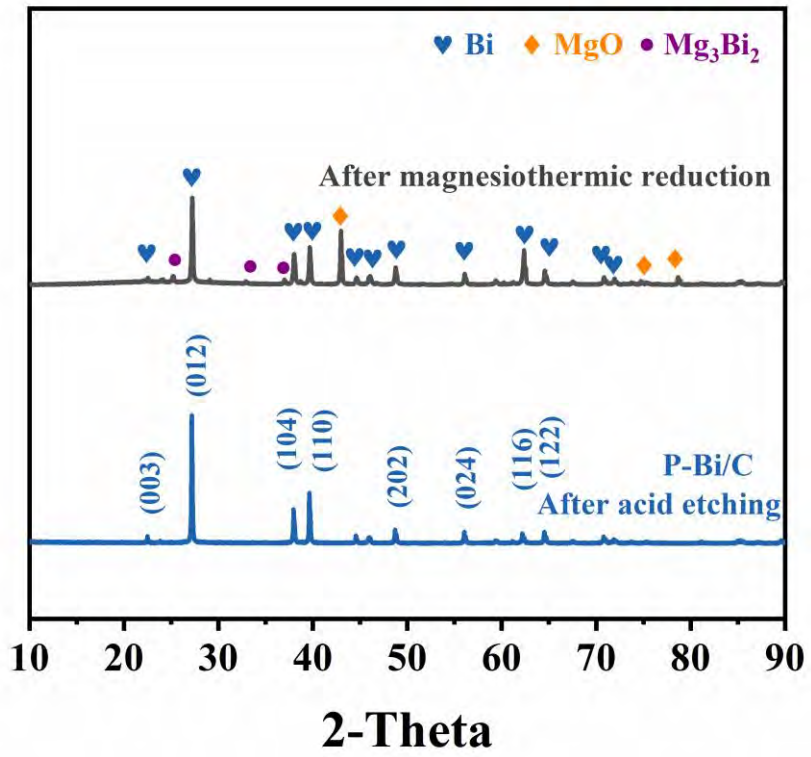

The corresponding reactions are:

$(BiO)_2CO_3=Bi_2O_3+CO_2$ (1)

$Bi_2O_3+3Mg=2Bi+3MgO$ $\Delta G_a = -1191.4$ KJ mol^{-1} (2)

$CO_2+2Mg=2MgO+C$ $\Delta G_a = -641.1$ KJ mol^{-1} (3)

a Calculated at 500 °C

Figure S2. XRD patterns of the products at different steps during preparation.

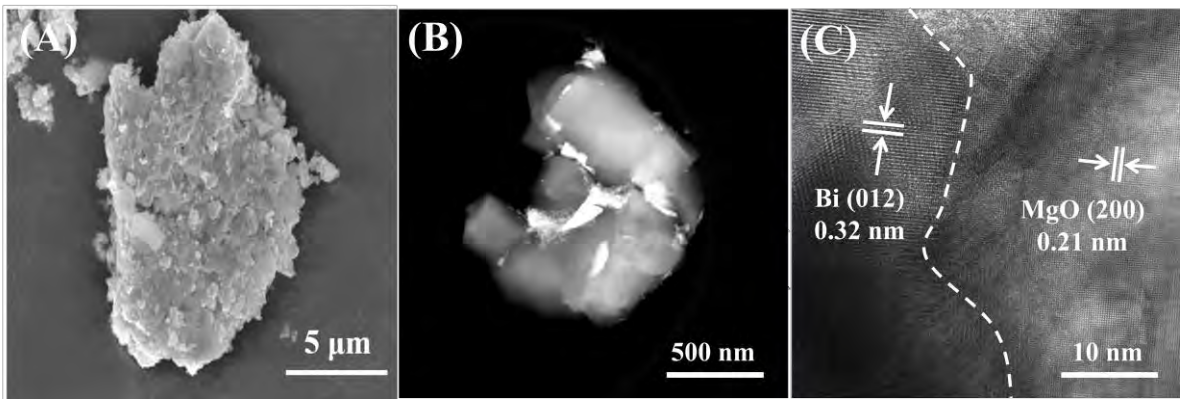

Figure S3. Morphological and structural characterization of Bi/MgO/C. A) SEM; B) STEM and C) HR-TEM images of the Bi/MgO/C heterostructure.

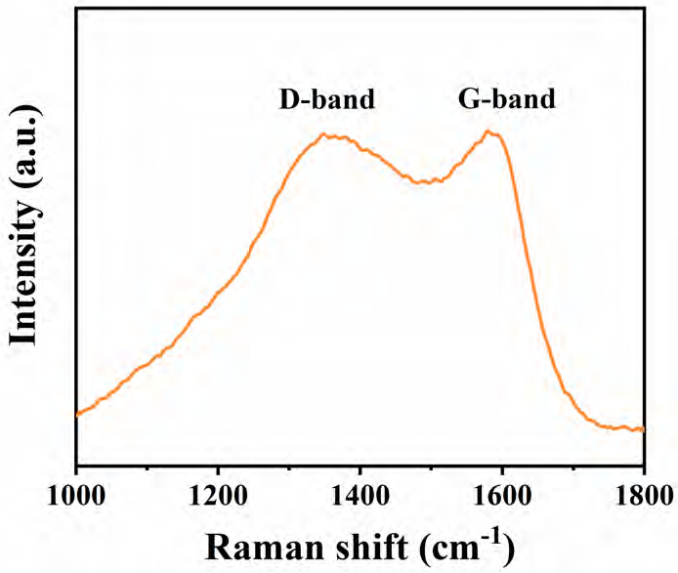

Figure S4. Raman scattering spectrum of MgO/Bi/MgO/C.

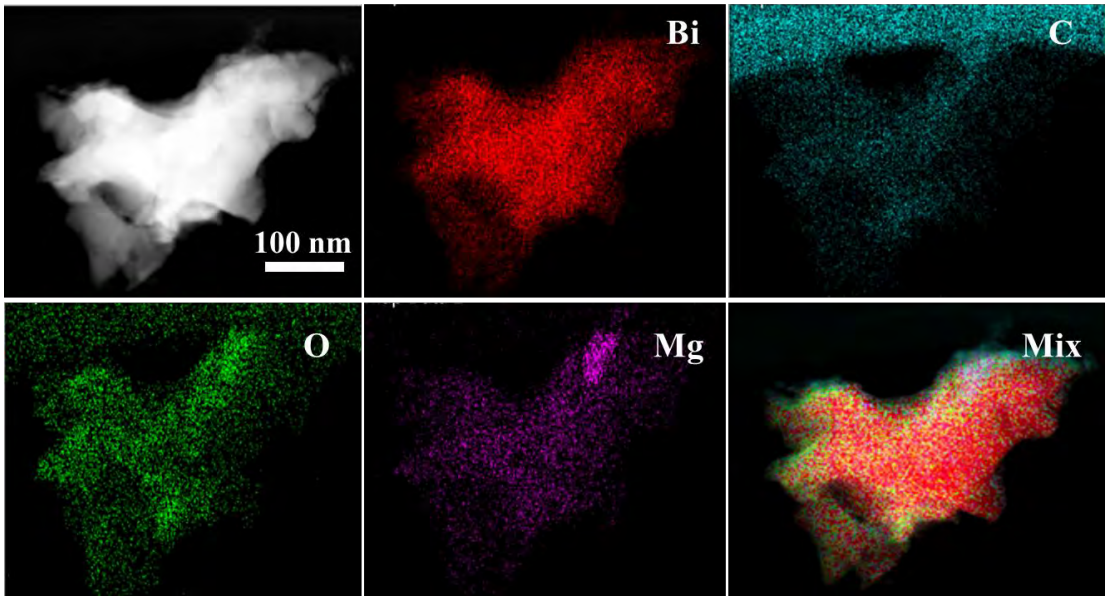

Figure S5. STEM and corresponding EDX mapping of MgO/Bi/MgO/C (scale bar=100 nm).

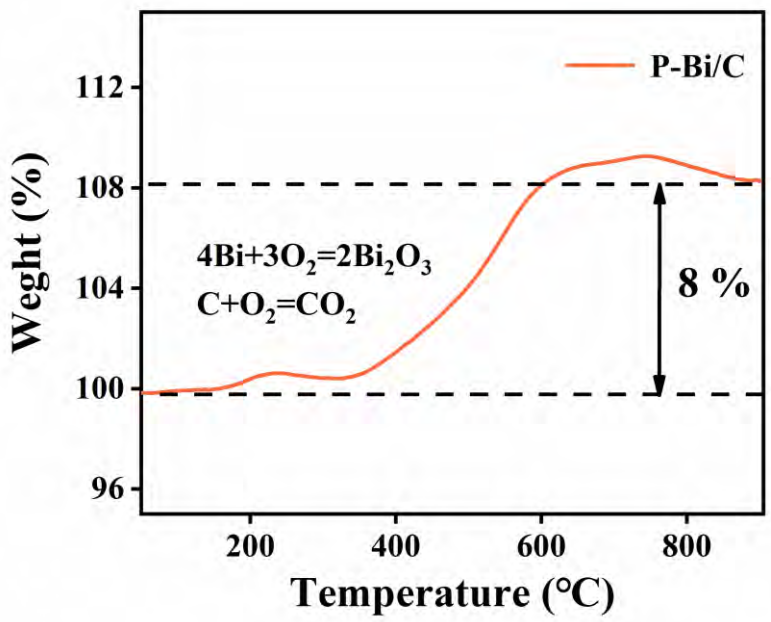

Figure S6. TGA curve of the P-Bi/C composite. Based on the theoretical Bi oxidation weight gain of 11%, the actual weight gain is 8% and so the carbon content is 3%.

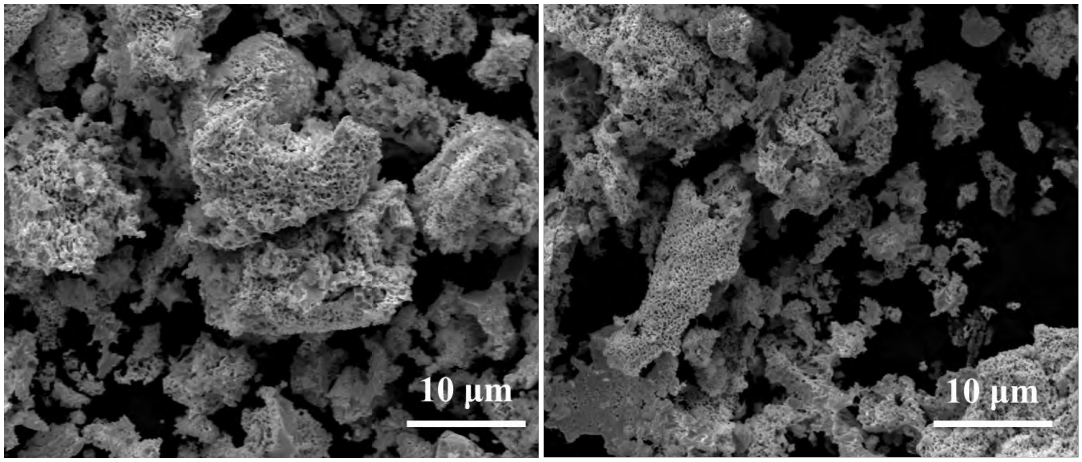

Figure S7. Different locations SEM images of P-Bi/C.

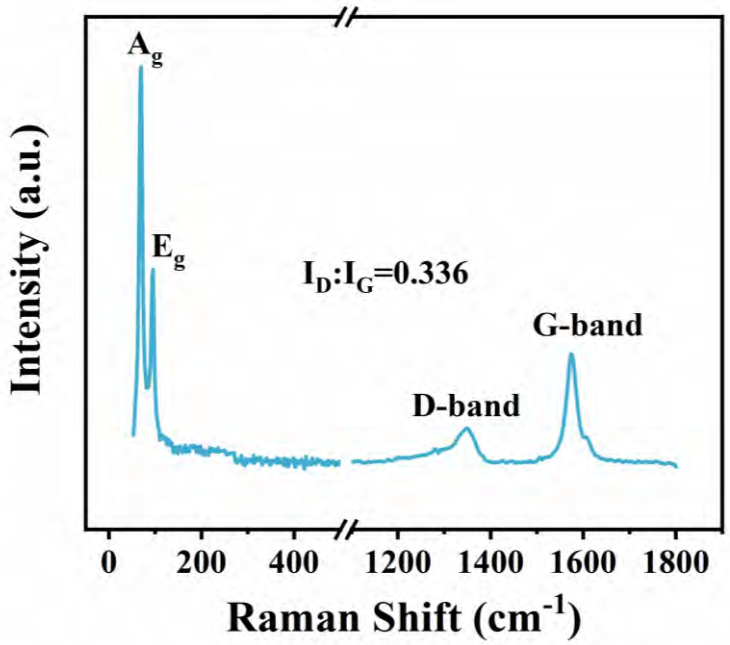

Figure S8. Raman spectra of P-Bi/C.

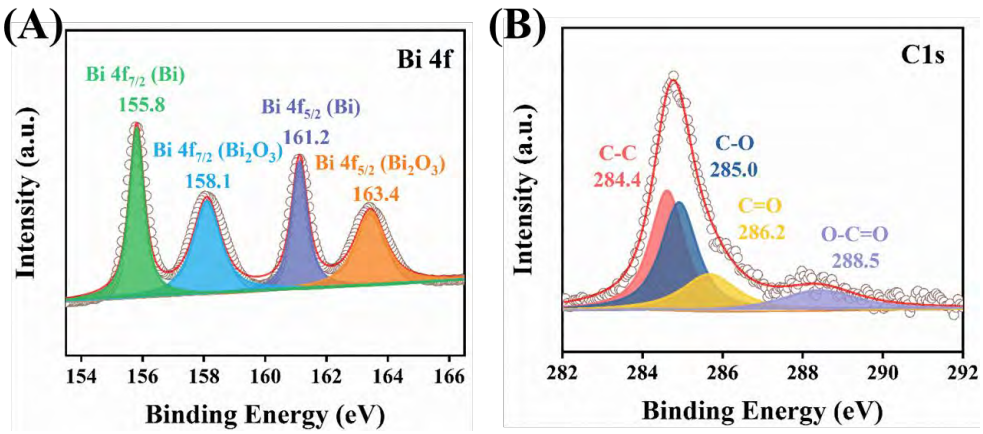

Figure S9. XPS spectra of P-Bi/C. A) Bi 1s and B) C 1s.

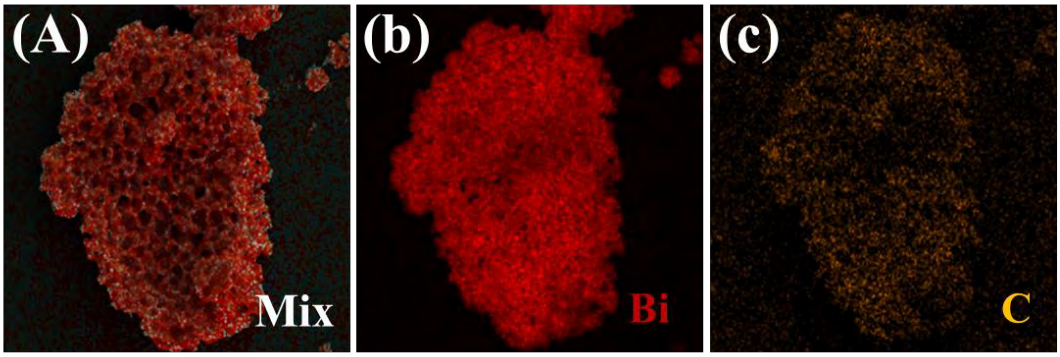

Figure S10. Elemental maps of P-Bi/C. A) The uniform distribution of C; B) Bi and C) C.

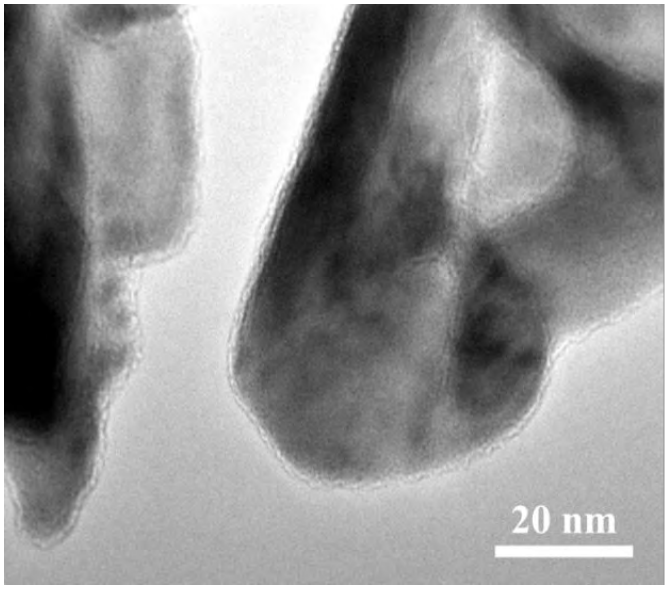

Figure S11. HR-TEM images of P-Bi/C composite.

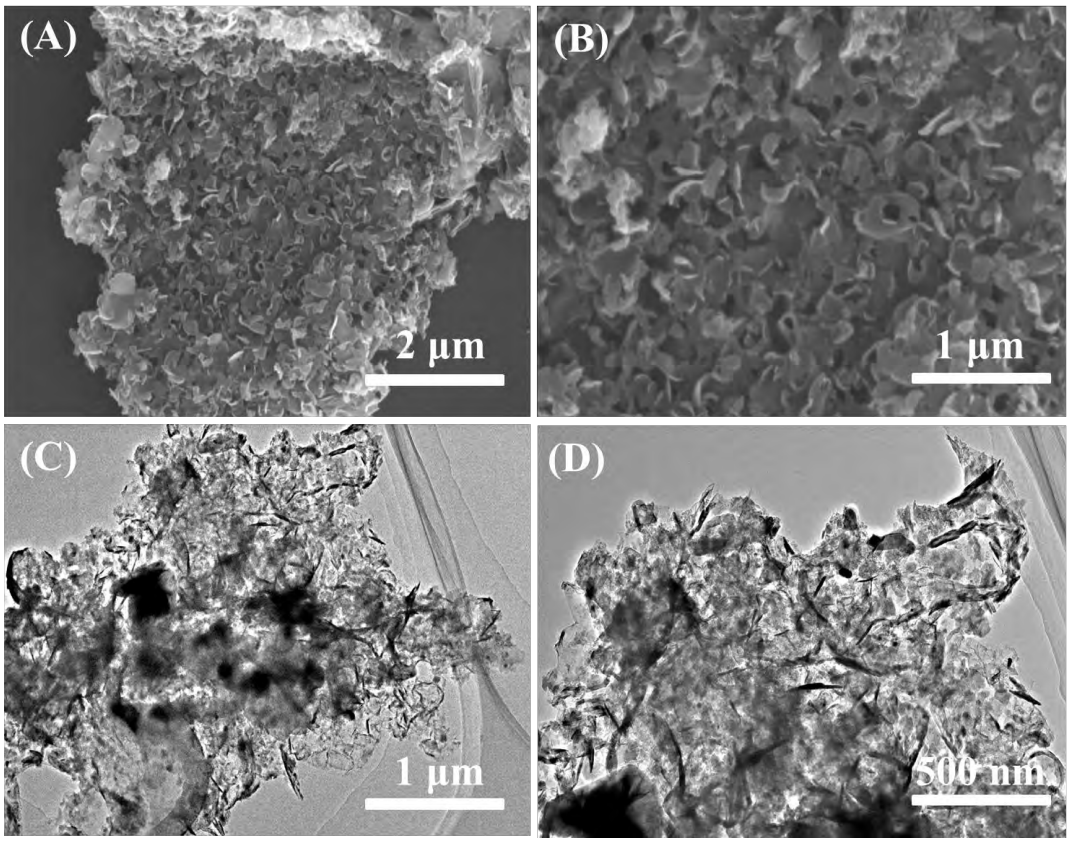

Figure S12. SEM and TEM image of P-Bi/C acid-etched with aqua regia ($V_{HCl:}$ V_{HNO3} = 3:1). A) SEM; B) Higher-magnification SEM images of C; C) TEM; D) Higher-magnification TEM images of C.

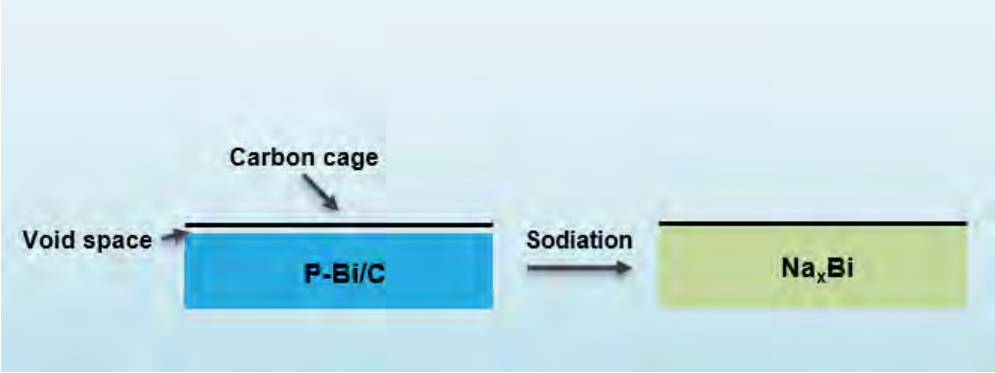

Figure S13. Schematic illustration of the sodiation process of P-Bi/C.

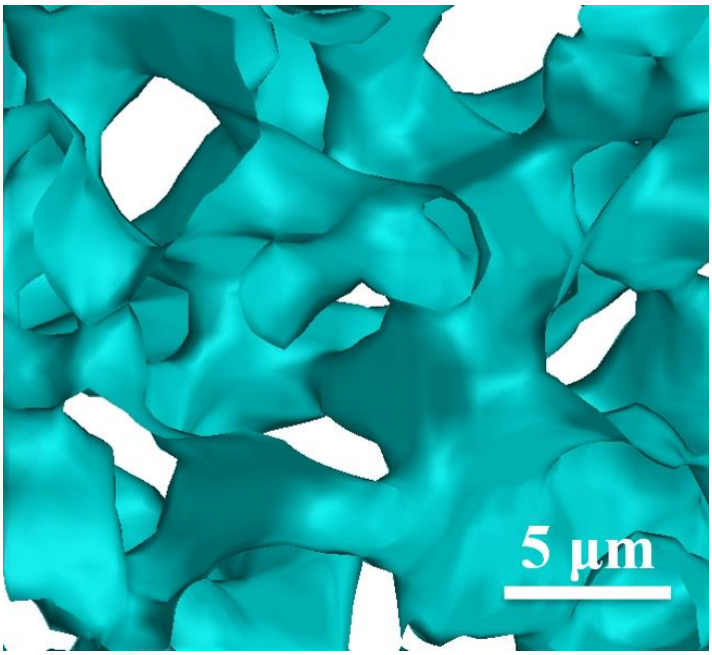

Figure S14. Sectional view of micro/nano-CT (Bulk volume of P-Bi/C = 2737.84 μm^3, pore volume = 1115.6 μm^3, and porosity = 40.8%).

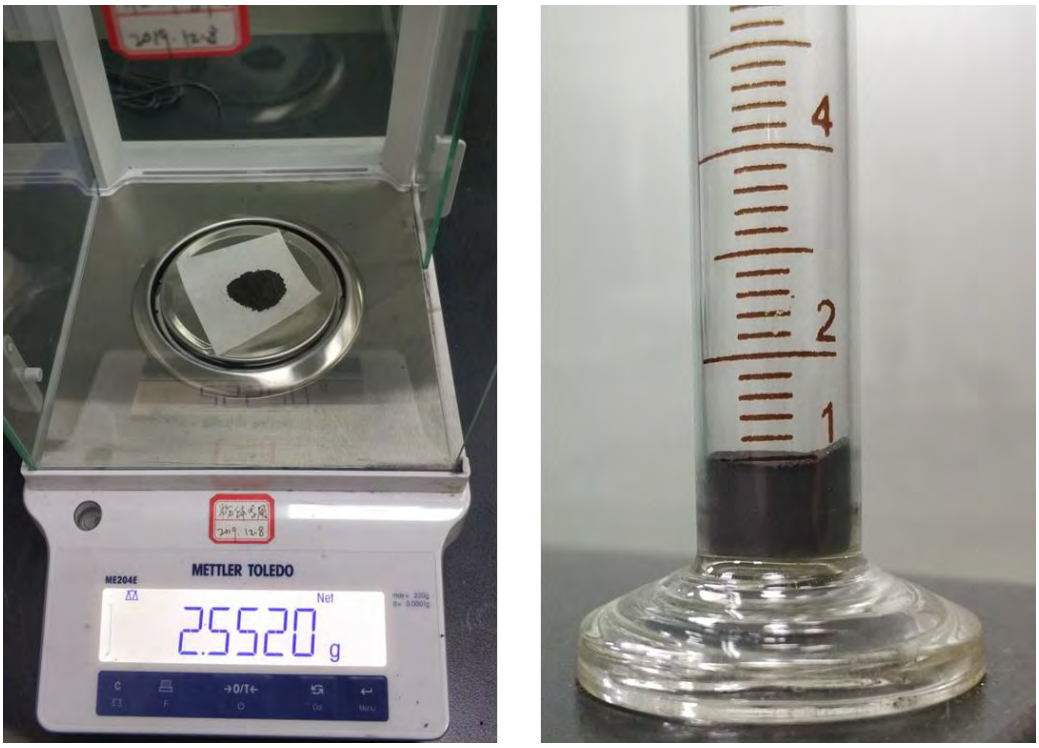

Figure S15. Photographs of the P-Bi/C powder (Mass = 2.55 g and tap density of P-Bi/C = 2.55 g cm^{-3}.

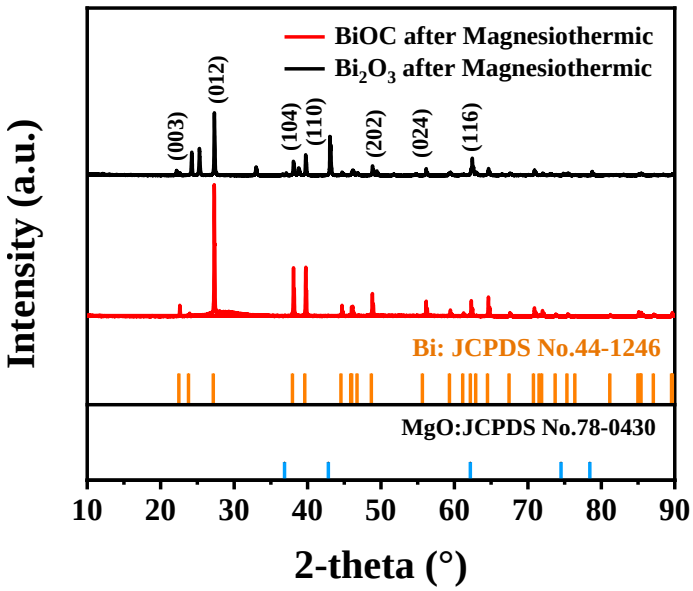

Figure S16. XRD patterns of Bi_2O_3+Mg.

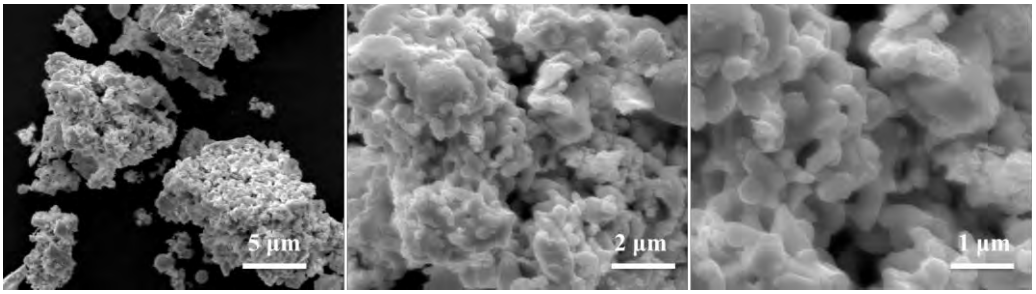

Figure S17. SEM images of porous Bi (P-Bi) at different resolutions.

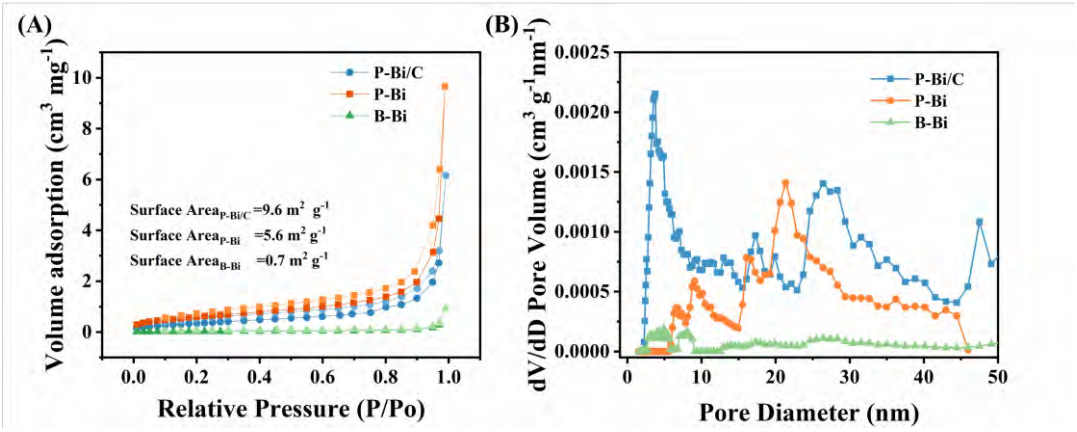

Figure S18. Porous structure characterization of samples. A) Nitrogen adsorption-desorption isotherms; B) Corresponding pore size distribution of bulk Bi, P-Bi, and P-Bi/C.

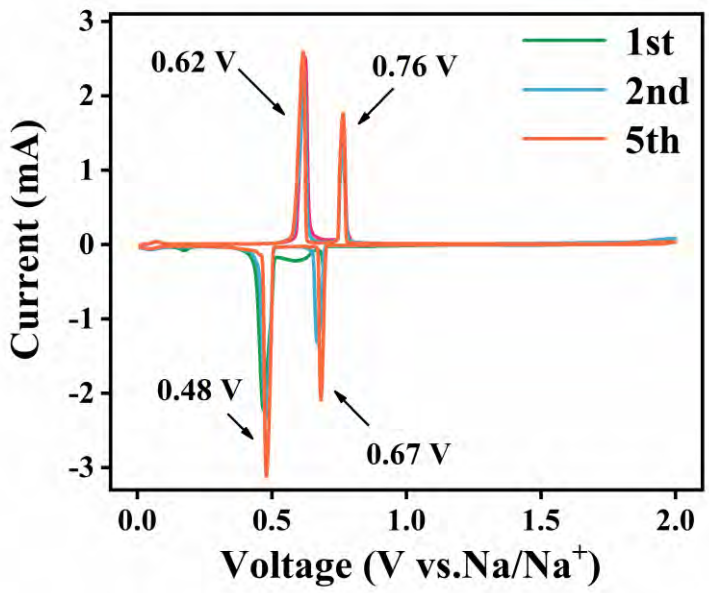

Figure S19. CV curves acquired at a scanning rate of 0.1 mV s^{-1} between 0.01 and 2 V.

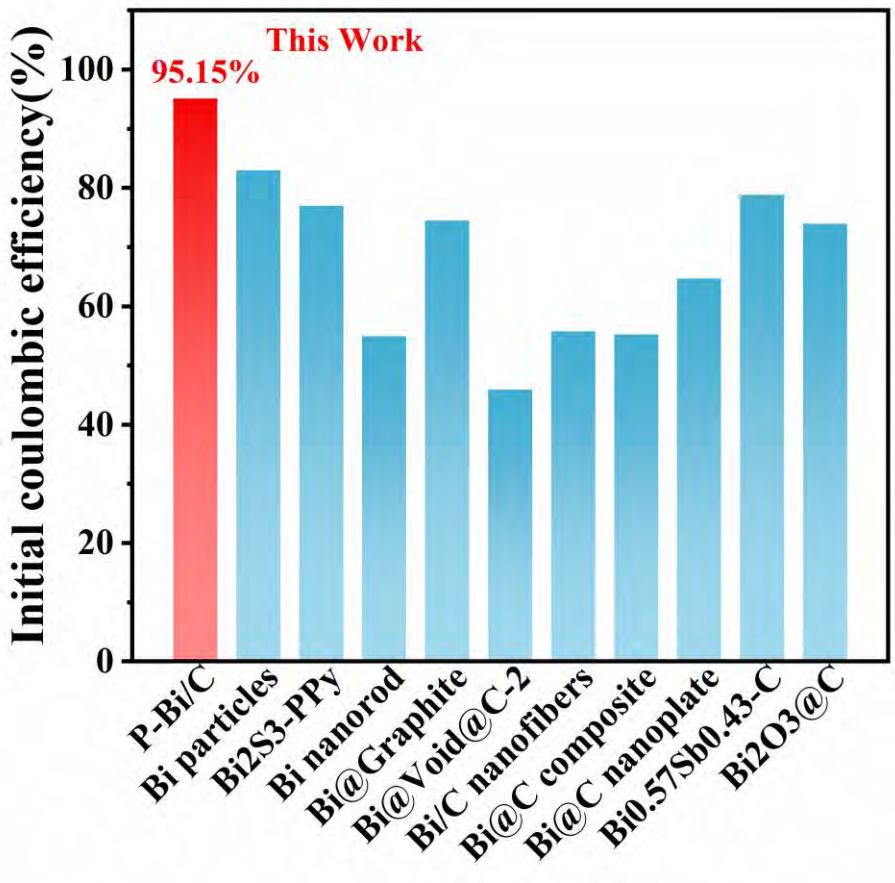

Figure S20. Initial CE values demonstrated here compared to those of other Bi-based anodes in the literature. [2-10]

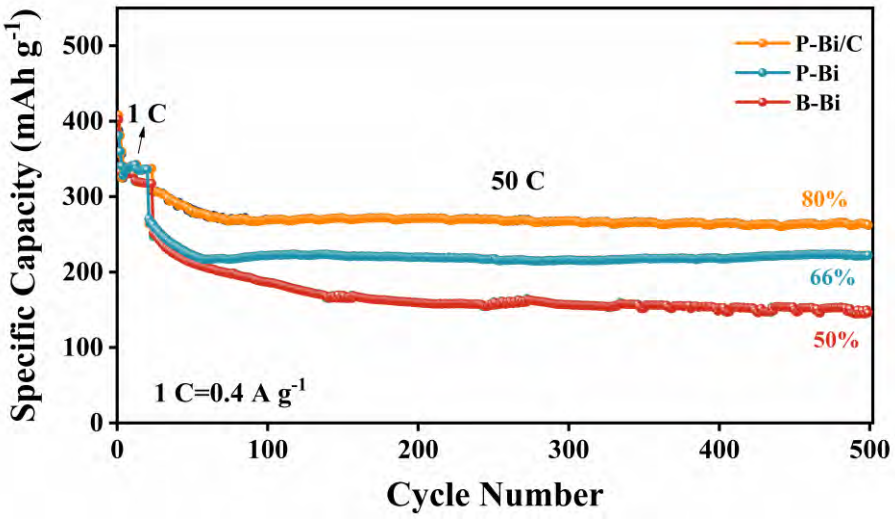

Figure S21. Cycling performance of the B-Bi, P-Bi and P-Bi/C for over 500 cycles at 50 C.

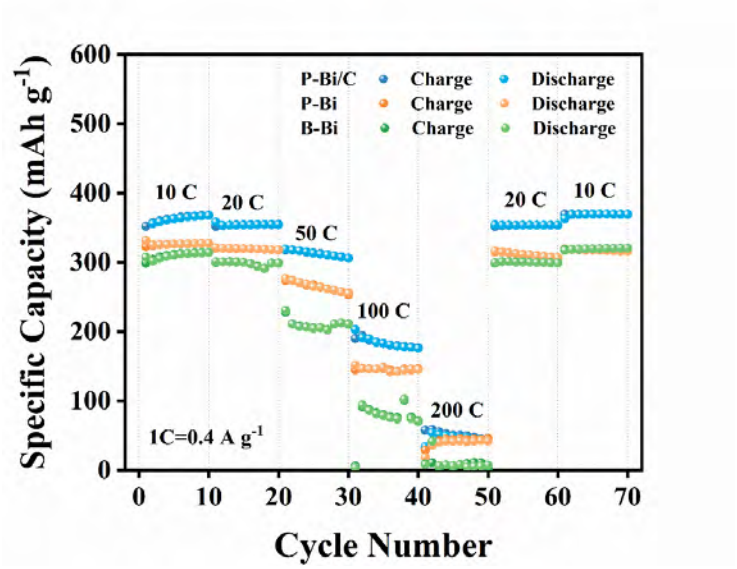

Figure S22. Rate properties of the B-Bi, P-Bi, and P-Bi/C electrodes at different current densities from 10 C to 200 C.

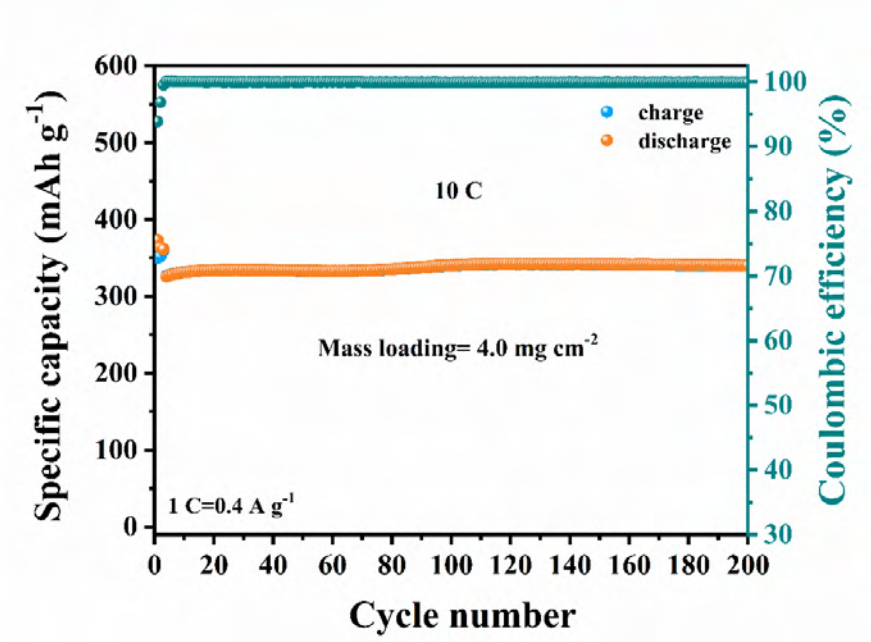

Figure S23. Specific capacities of the P-Bi/C anodes with mass loadings of 4.0 mg cm^{-2} at 10 C.

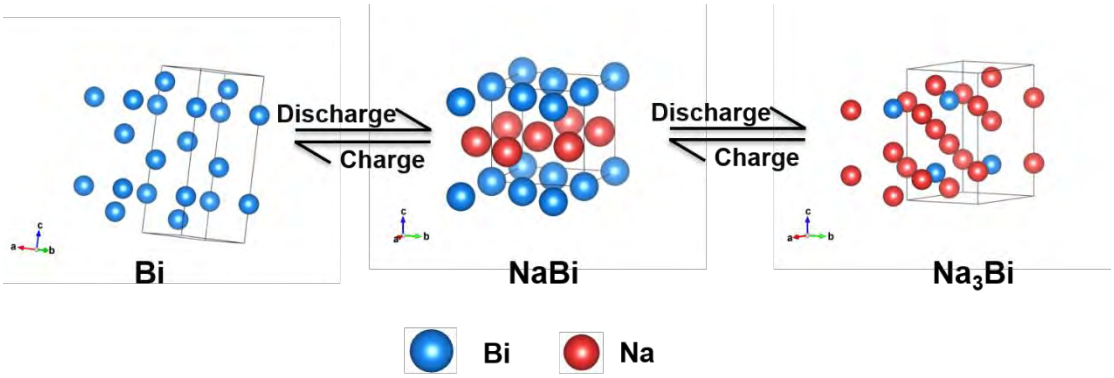

Figure S24. Schematic illustration showing the reaction mechanism of the P-Bi/C as an anode in SIBs in the initial discharging/charging cycle.

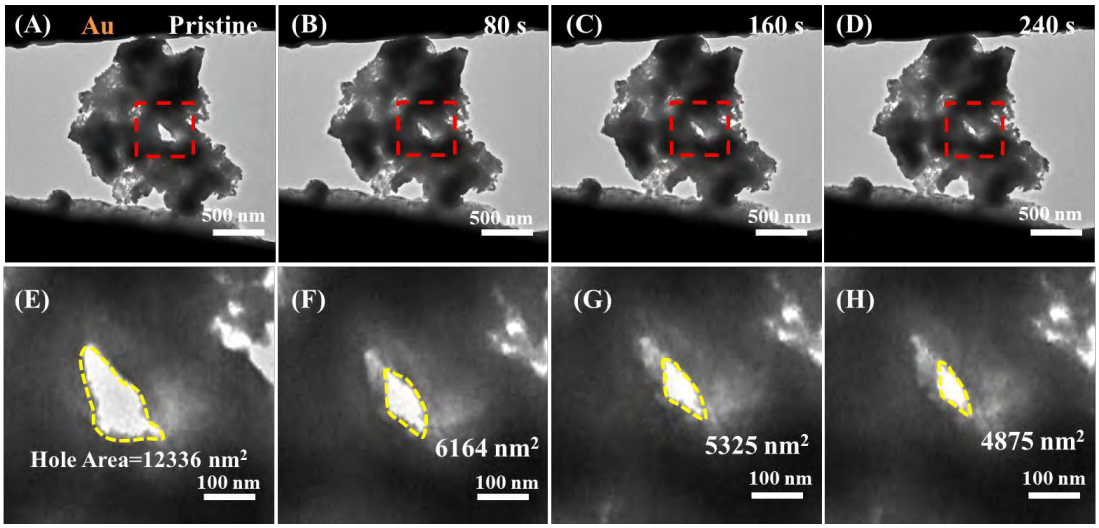

Figure S25. *In-situ* TEM images of P-Bi/C upon sodiation reveal the inner pore gradually shrink. (A-D) Time-resolved TEM images of P-Bi/C during the sodiation/desodiation process; (E-H) *In situ* TEM images of inner pore at the pristine state and after different sodiation/desodiation cycles.

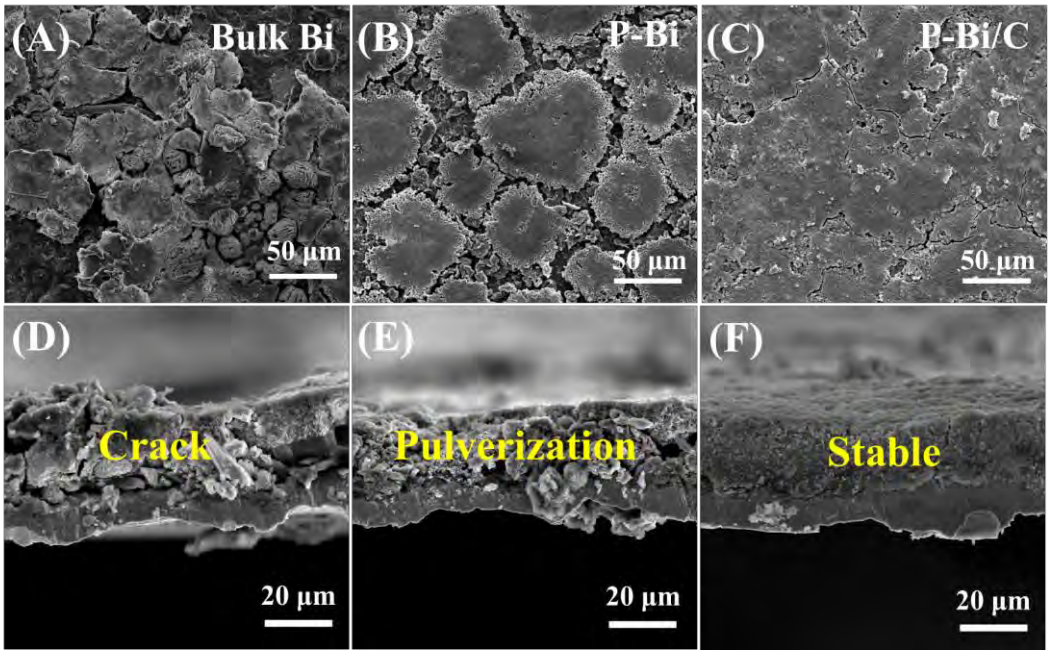

Figure S26. SEM image of P-Bi/C, P-Bi and B-Bi electrodes after cycling. Top-view SEM images of A) bulk Bi, B) P-Bi, and C) P-Bi/C and Cross-sectional SEM images of D) bulk Bi, E) P-Bi, and F) P-Bi/C.

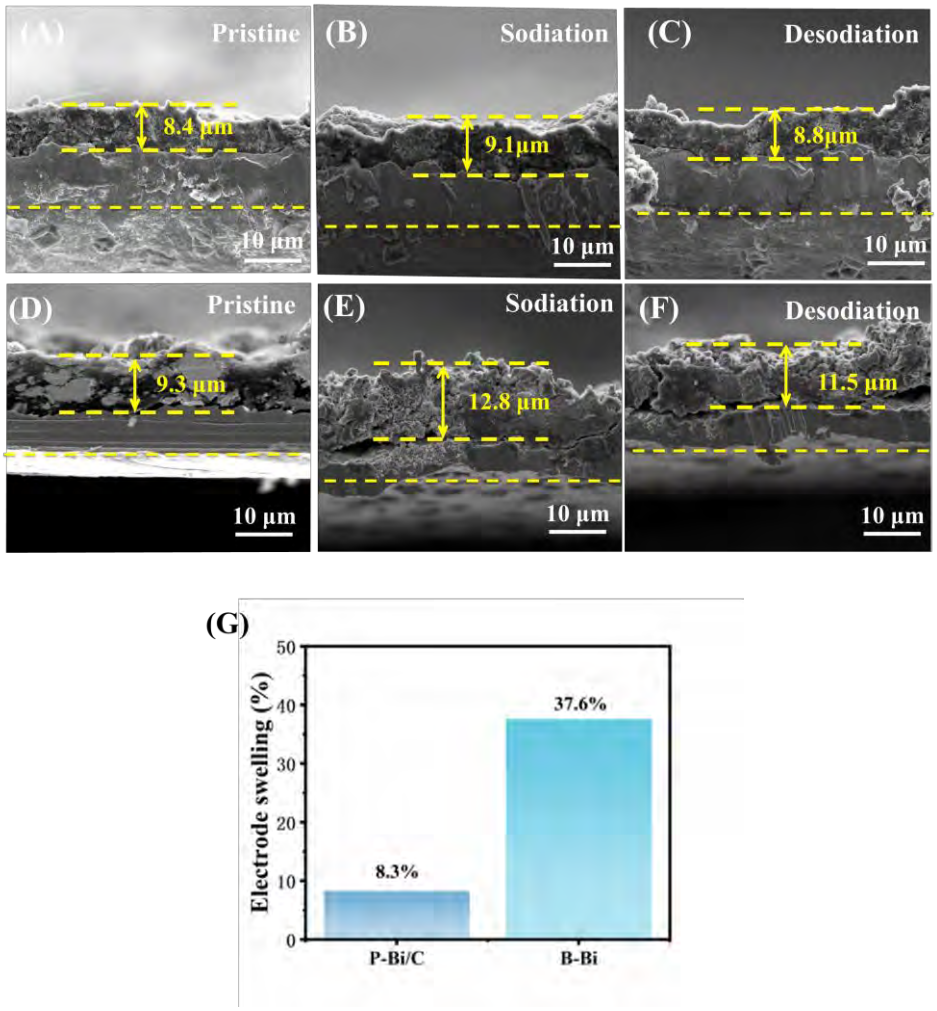

Figure S27. Electrode swelling measurements of P-Bi/C. (A-F) Cross-sectional SEM images acquired to investigate electrode swelling of P-Bi/C and B-Bi together with the corresponding cross-sectional SEM images after complete sodiation and desodiation; (G) Expansion rates of P-Bi/C and B-Bi after complete sodiation.

.

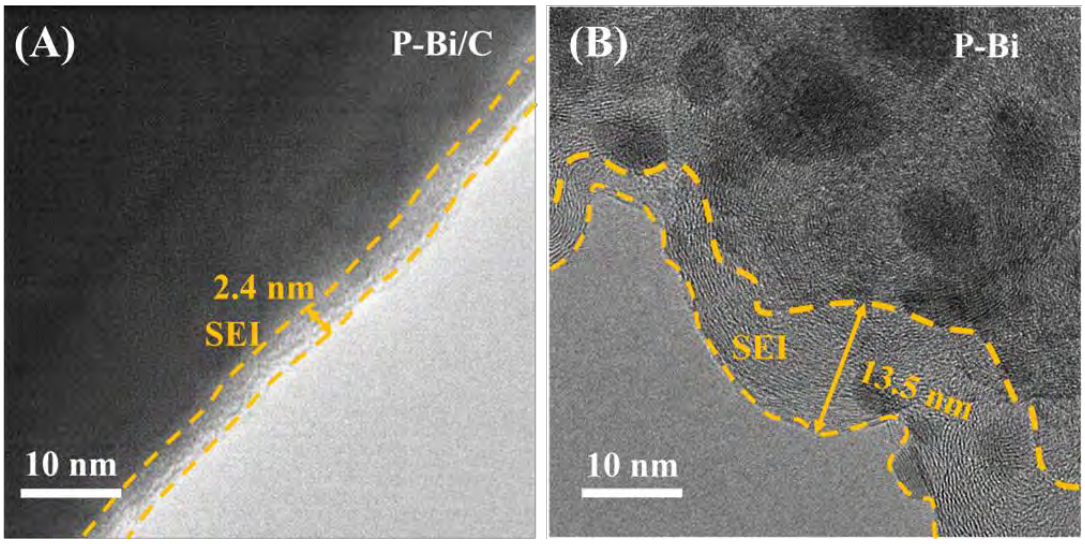

Figure S28. *Ex situ* HR-TEM images of the P-Bi/C and P-Bi anode after 500 cycles. A) Thin and tight SEI of P-Bi/C; B) Rough and thick SEI of P-Bi.

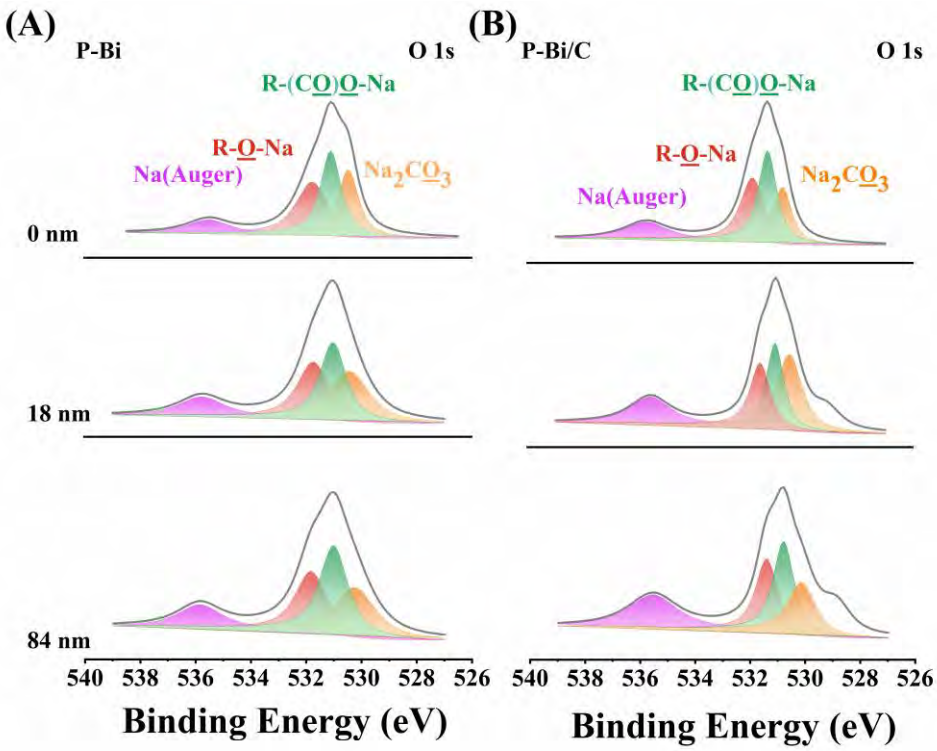

Figure S29. XPS depth profile of O 1*s* spectra for the P-Bi and P-Bi/C electrodes by Ar^+ sputtering. A) O 1*s* spectra of P-Bi; B) O 1*s* spectra of P-Bi/C.

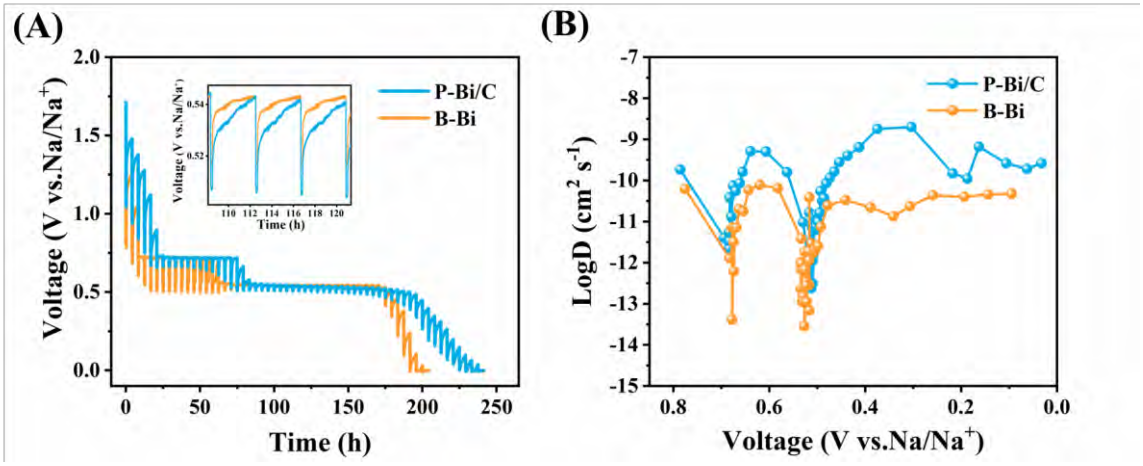

Figure S30. Na^+ diffusion coefficients calculated from GITT. A) The potential response curves of the P-Bi/C and P-Bi electrode during GITT measurements; B) Diffusion coefficients of in Na^+ calculated from GITT.

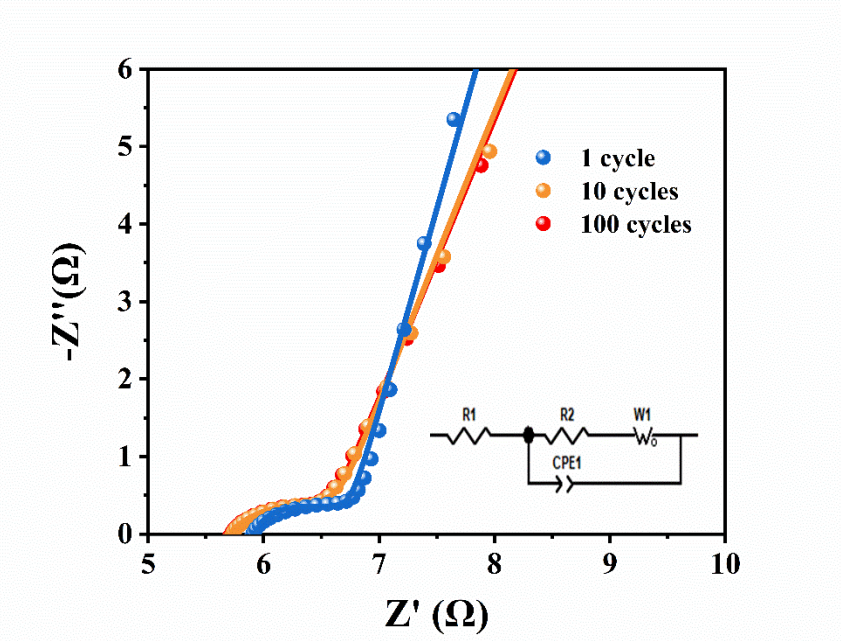

Figure S31. Nyquist plots and fitted lines of the P-Bi/C anode after different cycles.

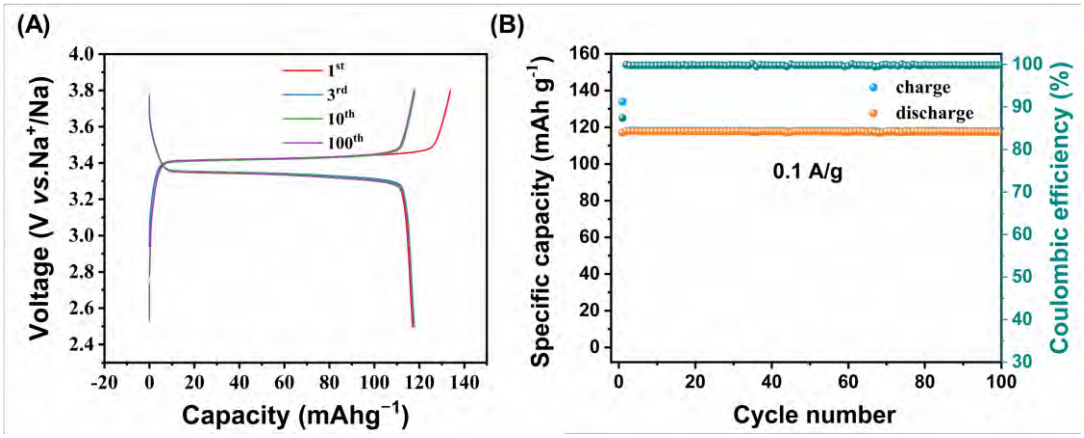

Figure S32. Electrochemical properties of the NVP//Na in half cells. A) The 1st, 3rd, 10th and 100th charging/discharging curves at 0.1 A g^{-1}; B) Cycling performances of NVP at 0.1 A g^{-1}.

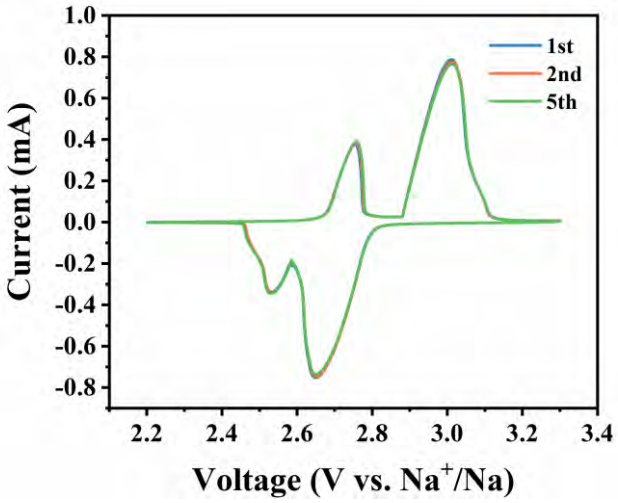

Figure S33. CV curves of the full SIB of P-Bi/C//NVP at 0.1 mV s^{-1}.

Table S1. Comparison of the electrochemical properties of different Bi-based anodes.

Materials	Tap density	Mass loading (mg/cm^2)	Cycling（mAh/g）	Rate capacity (mAh/g)	ICE (%)	Ref
This work	2.55	1.44~5.0	150 after 20000 cycles at 125C (50 A/g)	369.8 at 1 C (0.4 A/g) 101 at 180 C (72 A/g)	95.15%	
Bi@C nanoplates	-	0.5~1.75	~200 after 200 cycles at 0.15 A/g	74 at 2 A/g	64.7	[13]
Bulk-Bi	-	3	389 after 2000 cycles at 0.4 A/g	356 at 2 A/g	94.8	[14]
Bi@Void@C Nanospheres	-	1.0~2.0	198 after 10000 cycles at 20 A/g	173 at 100 A/g	46	[15]
Bi@C microspheres	-	0.95~1.01	123.5 after 100 cycles at 0.1 A/g	260 at 0.1 A/g 83.4 at 2 A/g	45	[16]
Bi@3DGFs	-	1.0	201 after 1500 cycles at 1 A/g	230 at 0.1 A/g 194 at 20 A/g	51.5	[17]
PBCNSs	-	0.6~1.2	340 after 16000 cycles at 20 A/g	400.3 at 0.2 A/g 372.8 at 25 A/g	~40	[18]
Bi@C composite	-	0.8~1.0	265 after 30000 cycles at 8 A/g	232 at 60 A/g	50.3	[19]

Bi-RGO	0.3	1.3~1.5	200 after 50 cycles at 0.05 A/g	~225 at 0.05 A/g ~0 at 5 A/g	-	[20]
$Bi_{0.57}Sb_{0.43}$-C	1.8	~1.77	293 after 50 cycles at 0.1 A/g	393 at 0.1 A/g 326 at 1A/g	78.9	[21]
$Bi_{0.7}Sb_{0.3}$ (MOF-836)	-	1.3~1.7	259.8 after 500 cycles at 0.2 A/g	486.4 at 0.025 A/g 285.1 at 2 A/g	76.7	[22]
Bi_2Sb_6	-	0.6~1	150 after 10000 cycles at 1 A/g	523.9 at 1 A/g 403.0 at 10 A/g	69.8	[23]
Bi/Ni	-	0.8~1.5	302.4 after 100 cycles at 0.2 A/g	377.1 at 0.02 A/g 206.4 at 2 A/g	-	[24]
Bi_2Te_3/Graphene	1.56	1.1~15	197 after 500 cycles at 2 A/g	229.2 at 2 A/g	90.1	[25]
Bi_2Se_3/GNS	2.07	1.28	183 after 1000 cycles at 10 A/g	181 at (10 A/g)	94.8	[26]
Bi2Se3/C	-	1.2~1.6	383 after 180 cycles at 0.1 A/g	500 at 0.1 A/g 186 at 10 A/g	75	[27]
BS-BO	-	0.41	109 after 50 cycles at 0.2 A/g	620 at 0.05 A/g 314 at 2 A/g	69.5	[28]
Bi_2S_3-PPy-HS	-	1.5	~320 after 5000 cycles at 1 A/g	365 at 0.1 A/g 278 at 3 A/g	70	[29]
Bi_2S_3/MXene	-	0.8~1.2	155 after 250 cycles at	407 at 0.1 A/g 168 at 5 A/g	-	[30]

BiOCl/RGO	-	-	0.5 A/g 266.6 after 100 cycles at 0.05 A/g	-	76.3	[31]

Table S2. Calculated impedance parameters for cycling of P-Bi/C.

	Rs(Ω)	*Rct(Ω)*
Fresh	7.71	20.08
1 cycle	6.28	9.02
10 cycles	5.71	1.03
100 cycles	5.93	0.48

References

1. Wang, L., Li, X., Jin, Z., Liang, Z., Peng, X., Ren, X., Gao, B., Feng, G., Chu, P., and Huo, K. (2019). Spatially controlled synthesis of superlattice-like SnS/nitrogen-doped graphene hybrid nanobelts as high-rate and durable anode materials for sodium-ion batteries. J. Mater. Chem. A *7*, 27475-27483.
2. Xiong, P., Bai, P., Li, A., Li, B., Cheng, M., Chen, Y., Huang, S., Jiang, Q., Bu, X., and Xu, Y. (2019). Bismuth nanoparticle@carbon composite anodes for ultralong cycle life and high-rate sodium-ion batteries. Adv. Mater. *31*, 1904771.
3. Wang, C., Wang, L., Li, F., Cheng, F., and Chen, J. (2017). Bulk bismuth as a high-capacity and ultralong cycle-life anode for sodium-ion batteries by coupling with glyme-based electrolytes. Adv. Mater. *29*, 1702212.
4. Yang, H., Chen, L., He, F., Zhang, J., Feng, Y., Zhao, L., Wang, B., He, L., Zhang, Q., and Yu, Y. (2017). Optimizing the void size of yolk-shell Bi@void@C nanospheres for high-power-density sodium-ion batteries. Nano Lett. *20*, 758-767.
5. Yuan, H., Jin, Y., Chen, X., Lan, J., Yu, Y., and Yang, X. (2019). Large-scale fabrication of egg-carton-inspired Bi/C composite toward high volumetric capacity and long-life lithium ion batteries. ACS Sustain. Chem. Eng. *7*, 6033-6042.
6. Xie, F., Zhang, L., Chen, B., Chao, D., Gu, Q., Johannessen, B., Jaroniec, M., and Qiao, S. (2019). Revealing the origin of improved reversible capacity of dual-shell bismuth boxes anode for potassium-ion batteries. Matter *1*, 1681-1693.
7. Xu, X., Wang, Z., Zhang, D., Zuo, S., Liu, J., and Zhu, M. (2020). Scalable one-pot synthesis of hierarchical Bi@C bulk with superior lithium-ion storage performances. ACS Appl. Mater. Interfaces *12*, 51478-5148.
8. Hong, W., Ge, P., Jiang, Y., Yang, L., Tian, Y., Zou, G., Cao, X., Hou, H., and Ji, X. (2019). Yolk-shell-structured bismuth@N-doped carbon anode for lithium-ion battery with high volumetric capacity. ACS Appl. Mater. Interfaces *11*, 10829-10840.
9. Qi, S., Xie, X., Peng, X., Ng, D., Wu, M., Liu, Q., Yang, J., and Ma, J. (2019). Mesoporous carbon-coated bismuth nanorods as anode for potassium-ion batteries. Phys. Status Solidi RRL *13*, 1900209.
10. Chen, J., Fan, X., Ji, X., Gao, T., Hou, S., Zhou, X., Wang, L., Wang, F., Yang, C., Chen, L., and Wang, C. (2018). Intercalation of Bi nanoparticles into graphite results in an ultra-fast and ultra-stable anode materials for sodium-ion batteries. Energy Environ. Sci. *11*, 1218-1225.
11. Song, G., Cheong, J. Y., Kim, C., Luo, L., Hwang, C., Choi, S., Ryu, J., Kim, S., Song, W. J., Song, H. K., Wang, C., Kim, I., and Park, S. (2019). Atomic-scale combination of germanium-zinc nanofibers for structural and electrochemical evolution. Nat. Commun. *10*, 2364.
12. Xiao, Z., Lei, C., Yu, C., Chen, X., Zhu, Z., Jiang, H., and Wei, F. (2020). Si@Si_3N_4@C composite with egg-like structure as high-performance anode material for lithium ion batteries. Energy Storage Mater. *24*, 565-573.
13. Xiang, J., Liu, Z., and Song, T. (2018). Bi@C nanoplates derived from $(BiO)_2CO_3$ as an enhanced electrode material for lithium/sodium-ion batteries. Chem. Sel. *3*, 8973-8979.

14. Wang, C., Wang, L., Li, F., Cheng, F., and Chen, J. (2017). Bulk bismuth as a high-capacity and ultralong cycle-life anode for sodium-ion batteries by coupling with glyme-based electrolytes. Adv. Mater. *29*, 1702212.
15. Yang, H., Chen, L. W., He, F., Zhang, J., Feng, Y., Zhao, L., Wang, B., He, L., Zhang, Q., and Yu, Y. (2020). Optimizing the void size of yolk-shell Bi@void@C nanospheres for high-power-density sodium-ion batteries. Nano lett. *20*, 758-767.
16. Yang, F., Yu, F., Zhang, Z., Zhang, K., Lai, Y., and Li, J. (2016). Bismuth nanoparticles embedded in carbon spheres as anode materials for sodium/lithium-ion batteries. Chem. *22*, 2333-2338.
17. Cheng, X., Li, D., Wu, Y., Xu, R., and Yu, Y. (2019). Bismuth nanospheres embedded in three-dimensional (3D) porous graphene frameworks as high performance anodes for sodium- and potassium-ion batteries. J. Mater. Chem. A *7*, 4913-4921.
18. Zhu, J., Wang, J., Li, G., Huang, L., Cao, M., and Wu, Y. (2020). Heterogeneous structured pomegranate-like Bi@C nanospheres for high-performance sodium storage. J. Mater. Chem. A *8*, 25746-25755.
19. Xiong, P., Bai, P., Li, A., Li, B., Cheng, M., Chen, Y., Huang, S., Jiang, Q., Bu, X., and Xu, Y. (2019). Bismuth nanoparticle@carbon composite anodes for ultralong cycle life and high-rate sodium-ion batteries. Adv. Mater. *31*, 1904771.
20. Hwang, J., Park, J.H., Yoon Chung, K., and Kim, J. (2020). One-pot synthesis of Bi-reduced graphene oxide composite using supercritical acetone as anode for Na-ion batteries. Chem. Eng. J. *387*,124111.
21. Zhao, Y., and Manthiram, A. (2015). High-capacity, high-rate Bi-Sb alloy anodes for lithium-ion and sodium-ion batteries. Chem. Mater. *27*, 3096-3101.
22. Zhang, W., Yan, W., Jiang, H., Wang, C., Zhou, Y., Ke, F., Cong, H., and Deng, H. (2019). Uniform Bi-Sb alloy nanoparticles synthesized from MOFs by laser metallurgy for sodium-ion batteries. ACS sustain. chem. eng. *8*, 335-342.
23. Gao, H., Niu, J., Zhang, C., Peng, Z., and Zhang, Z. (2018). A dealloying synthetic strategy for nanoporous bismuth-antimony anodes for sodium ion batteries. ACS Nano *12*, 3568-3577.
24. Wang, L., Wang, C., Li, F., Cheng, F., and Chen, J. (2018). In situ synthesis of Bi nanoflakes on Ni foam for sodium-ion batteries. Chem. Commun. *54*, 38-41.
25. Sun, D., Zhang, G., Li, D., Liu, S., Jia, X., and Zhou, J. (2019). A layered Bi_2Te_3 nanoplates/graphene composite with high gravimetric and volumetric performance for Na-ion storage. Sustain. Energy Fuels *3*, 3163-3171.
26. Li, D., Zhou, J., Chen, X., and Song, H. (2018). Graphene-loaded Bi_2Se_3: a conversion-alloying-type anode material for ultrafast gravimetric and volumetric Na storage. ACS Appl. Mater. Interfaces *10*, 30379-30387.
27. Xie, L., Yang, Z., Sun, J., Zhou, H., Chi, X., Chen, H., Li, A. X., Yao, Y., and Chen, S. (2018). Bi_2Se_3/C nanocomposite as a new sodium-ion battery anode material. Nanomicro Lett. *10*, 1-9.
28. Lei, K., Wang, C., Liu, L., Luo, Y., Mu, C., Li, F., and Chen, J. (2018). A porous network of bismuth used as the anode material for high-energy-density potassium-ion batteries. Angew. Chem. Int. Ed. *57*, 4687-4691.

29. Long, B., Qiao, Z., Zhang, J., Zhang, S., Balogun, M-S., Lu, J., Song, S., and Tong, Y. (2019). Polypyrrole-encapsulated amorphous Bi_2S_3 hollow sphere for long life sodium ion batteries and lithium–sulfur batteries. J. Mater. Chem. A *7*, 11370-11378.
30. Yang, Q., Gao, W., Zhong, W., Tao, M., Qi, Y., Bao, S., and Xu, M. (2020). A synergistic Bi_2S_3/MXene composite with enhanced performance as an anode material of sodium-ion batteries. New J. Chem. *44*, 3072-3077.
31. Sun, J., Tu, W., Chen, C., Plewa, A., Ye, H., Sam Oh, J. A., He, L., Wu, T., Zeng, K., and Lu, L. (2019). Chemical bonding construction of reduced graphene oxide-anchored few-layer bismuth oxychloride for synergistically improving sodium-ion storage. Chem. Mater. *31*, 7311-7319.